Immobilization of Hairpin Deoxyribose Nucleic Acid Aptamers on Gold: Surface Folding Dictated Analyte-Binding Performance and Electron Transfer Kinetics

by

Cassie Ho

B.Sc. (Chemistry), Simon Fraser University, 2005

THESIS SUBMITTED IN PARTIAL FULFILLMENT
OF THE REQUIREMENTS FOR THE DEGREE OF
MASTER OF SCIENCE

in the
Department of Chemistry
Faculty of Science

SIMON FRASER UNIVERSITY

Winter 2011

Approval

Name: **Cassie Ho**

Degree: **Master of Science (Chemistry)**

Title of Thesis: ***Immobilization of hairpin DNA aptamers on gold: surface folding dictated analyte-binding performance and electron transfer kinetics***

Examining Committee:

Chair: Dr. Krzysztof Starosta, Associate Professor

Dr. Hua-Zhong (Hogan) Yu
Senior Supervisor
Professor

Dr. Steven Holdcroft
Supervisor
Professor

Dr. Peter Unrau
Supervisor
Associate Professor

Dr. Charles Walsby
Internal Examiner
Associate Professor
Department of Chemistry

Date Defended/Approved: November 28, 2011

Partial Copyright Licence

Abstract

The performance of hairpin aptamer-based electrochemical sensors is highly dependent on the structural nature of the DNA aptamer monolayer immobilized on the electrode surface. It was discovered in this study that an increase of the surface density of aptamers on the electrode does not improve the sensor's sensitivity, but in fact diminishes its response to the analyte. The electron transfer kinetics between the redox centre (methylene blue) and the gold electrode strongly depend on the surface density (and thus the folding state) of the hairpin DNA aptamers, and shows a unique two-stage behaviour, i.e., a relatively fast process (irrespective of the surface density) at low surface density followed by a sharp decrease in the apparent rate constants (when the surface density increases).

Keywords: biosensor; DNA; aptamer; electrochemistry; biomarker; cancer

To my family and friends

Acknowledgements

Firstly, I would like to thank Dr. S. Holdcroft and Dr. P.J. Unrau for being on my committee – their advice and suggestions have been tremendously helpful to my work. I would also like to thank Dr. K. Starosta and Dr. C. Walsby for taking the time to be the chair and internal examiner at my defence.

I would also like to thank Dr. Jason Thomas and Dr. Banani Chakraborty for providing the NAP II proteins for my gel shift assays and for their valuable discussions on CTAP III, NAP II and EMSAs in general. Heartfelt thanks goes to Dr. Janet Huang for her helpful conversations on polyacrylamide gel electrophoresis and HPLC. I am very grateful to Dr. Dipankar Sen for allowing me to perform my EMSA experiments in his laboratory and the Sen research group for their kindness in providing me with bench space in their lab.

As well, I would like to thank my senior supervisor, Dr. Hua-Zhong (Hogan) Yu, for his guidance and support in the lab. I have learned a lot during the course of this degree and I have found Hogan's advice to be invaluable. I am very thankful to the past and present members of the Yu research group for their friendship.

Table of Contents

List of Figures

List of Acronyms

A	adenosine nucleoside
ACV	alternating current voltammetry
ALP	alkaline phosphatase
AQ	anthraquinone
ATP	adenosine triphosphate
C	cytidine nucleoside
CA	chronoamperometry
CP	chronopotentiometry
CRP	c-reactive protein
CTAP III	connective tissue-activating peptide III
CV	cyclic voltammetry
DI	diaphorase
DNA	deoxyribose nucleic acid
DPV	differential pulse voltammetry
dsDNA	double-stranded DNA
EDTA	ethylenediaminetetraacetic acid
ELISA	enzyme-linked immunosorbent assays
ESI	electrochemical impedance spectroscopy
ESI-MS	electrospray ionization-mass spectrometry
FRET	fluorescence resonance energy transfer
G	guanosine nucleoside
GA	glutaraldehyde
GDH	glucose dehydrogenase
HEPES	4-(2-hydroxyethyl)-1-piperazineethanesulfonic acid
HPLC	high pressure liquid chromatography
ITO	indium-tin oxide
LB	leucomethylene blue
LC-MS	liquid chromatography-mass spectrometry
m-PMS	1-methoxyphenazine methosulphate
MB	methylene blue
MCH	6-mercaptohexan-1-ol

MUC1	mucin-1
NADH	nicotinamide adenine dinucleotide
NAP II	neutrophil-activating peptide 2
nt	nucleotides
p-AP	p-aminophenol
p-APP	p-aminophenylphosphate
p-QI	p-quinonimine
PAMAM	G4-amino-terminated polyamindoamine dendrimer
PBP	platelet basic protein
PCR	polymer chain reaction
PQQ-GDH	pyrroquinoline quinone glucose dehydrogenase
PTFE	polytetrafluoroethylene
QD	quantum dot
RNA	ribose nucleic acid
SELEX	systematic evolution of ligands by exponential enrichment
ssDNA	single-stranded DNA
SWCNT	single-walled carbon nanotube
SWV	square-wave voltammetry
T	thymidine nucleoside
TBA	thrombin binding aptamer
TCEP	tris(2-carboxyethyl)phosphine
TFA	trifluoroacetic acid
UV	ultraviolet
VTR	variable tandem repeat

1. Introduction

This chapter is a general introduction to aptamers, aptamer-based sensors and electrochemical sensors. It will provide the fundamental concepts and recent research required to understand the work in this thesis.

1.1. Biosensors

Sensors are devices composed of three parts; a detection element, which responds to stimulus; a transduction element, which modifies the detection event to a signal; and a signaling element, which gives a readout for interpretation by the user. Biosensors are, as the name suggests, sensors that contain a biological element for detection. Biological processes are complex and it is often difficult to design detection elements with small molecule chemistry that will interact with large proteins, enzymes and other biological markers selectively. Biosensors take advantage of sensitive biological recognition reactions to discriminate against the target analyte amongst a large pool of biomolecules; as a result, well-designed biosensors have the potential to eliminate the need for sample processing prior to detection.

The ability to detect the presence of certain biomolecules inside the human body is essential in the assessment of a patient's health; these biomolecules, or biomarkers, can act as an indication of disease or illness inside the body. In modern healthcare, enzyme-link immunosorbent assays (ELISA) are the standard for biomarker detection. However, typical ELISAs require multistep protocols which necessitate the use of highly trained clinicians to perform, process and interpret the assay. The use of biosensors in place of ELISAs can potentially eliminate many of these preparation steps. The greatest advantage biosensors have over conventional laboratory processes is the biosensors'

potential to deliver point-of-care diagnosis. The ideal biosensors for this purpose should be light-weight, portable, require little to no sample manipulation prior to detection and should give easy-to-interpret results. In countries that lack strong healthcare infrastructures, biosensors have the ability to greatly improve the delivery of timely medical care.

Many types of signal transduction techniques are used in biosensors. However, the two that lends themselves best to adaptation for general usage are optical and electrochemical detection techniques. The relatively simple transformation of a target detection event into a measureable signal, combined with the low theoretical limit of detection, make optical and electrochemical sensors popular with researchers. However, electrochemical sensors have a greater potential for miniaturization compared with optical sensors due to their simple compatibility with the semiconductor components. The ubiquitous electrochemical glucose monitors are perhaps the best example of a successful commercial electrochemical biosensor[1-3] (Figure 1-1).

Figure 1-1: Portable glucose monitors

Commercial portable glucose monitor for use by patients at home with simple-to-read digital displays and attractive colors to appeal to consumers. Image adapted from reference [2].

1.2. Deoxyribose nucleic acids

Deoxyribose nucleic acid (DNA) is a polymer composed of four different monomer units: bases adenosine (A), cytidine (C), guanosine (G), and thymidine (T), that forms the basis of all life on earth (Figure 1-2)[4,5]. The anti-parallel double-helical structure of DNA, first proposed by Watson and Crick[6] in 1953, is held together by both hydrogen bonding between the complementary bases (A and T, and G and C)[7] and planar aromatic base stacking[8]. The charged hydrophilic phosphate backbone is wound around the periphery of the molecule with the hydrophobic purine and pyrimidine bases forming the core around a central axis[5]. Base stacking also plays a significant role in the structure of single-stranded DNA (ssDNA)[8].

Figure 1-2: Chemical structure of DNA

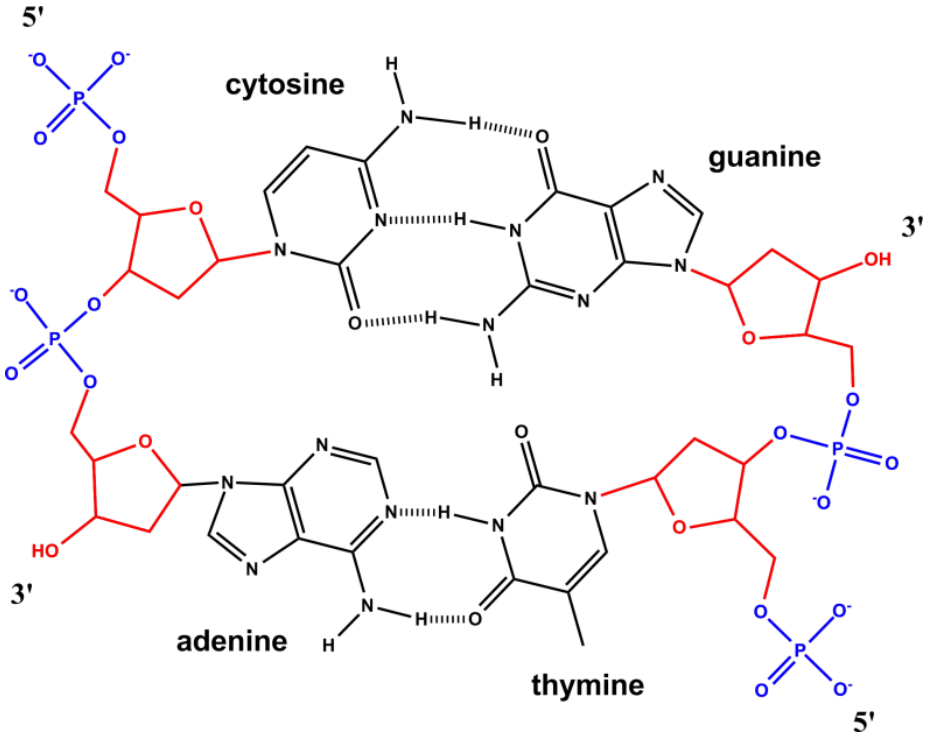

Chemical structure of DNA showing the ribose (red) and phosphate (blue) that forms the backbone, and the aromatic bases (black). Hydrogen bonding between the Watson-Crick base pairs is shown by the dashed lines.

There are three main structural forms of DNA. The A and B forms are right-handed helices while the Z form is a left-handed helix[9] (Figure 1-3). Although all three forms can be found in nature, the dominant form in biological systems is the B form[5]. In this form, the double helix has a diameter of approximately 23.7 Å and a base-pair distance of approximately 3.4 Å[4]. The helix completes one turn every 10 base-pairs (bp)[5].

Figure 1-3: 3-dimensional X-ray structures of A-, B-, and Z-DNA.

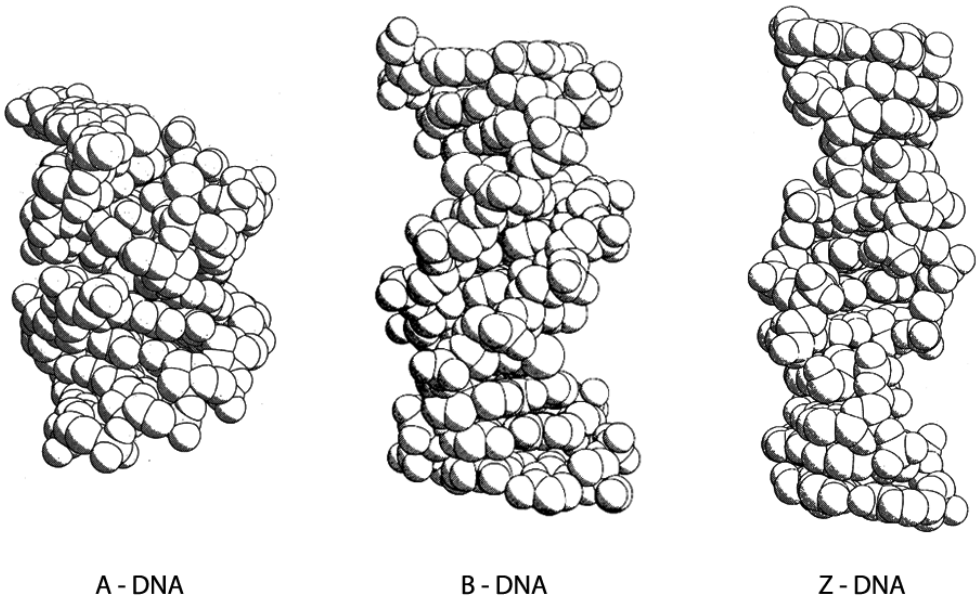

A-DNA has higher torsional strain around the central axis while B-DNA has less torsional strain. Unlike A- and B-DNA, Z-DNA is a left-handed helix. Figure adapted from reference [9].

1.3. Aptamers

Aptamers are artificially engineered oligonucleotides that bind to their target ligands with high specificity and affinity. They were first reported independently by Szostak[10] and Gold[11] back in 1990 and since then aptamers have been adapted for numerous applications ranging from the detection of small molecules in food and in the environment[12] to the identification of live parasites that infect humans[13] to being an integral part of targeted drug delivery systems[14,15]. Although the binding mechanism of

an aptamer to its target molecule is not clear in every case, it is suggested that aptamers bind by wrapping around their target and enveloping them[16,17] and, as a result, the name aptamer is derived from the Latin word *aptus* (meaning “to fit”). One of the benefits of aptamers is that it is possible to select an aptamer for any target, even targets whose structure is entirely unknown, with *in vitro* selection[18,19].

Compared to antibodies, aptamers have many advantages that make them more suitable for use as the sensing element in biosensors. Aptamers tend to be less toxic and less immunogenic than antibodies[20] and will clear the body in a relatively short time frame[20]. They also do not require an immune response in host animals to be produced; aptamers are commonly produced chemically in an oligonucleotide synthesizer in large quantities. This allows aptamers to be produced against toxic ligands that cannot survive in a host animal. In addition, aptamers will often have sub-micromolar affinities to their targets that are comparable to antibodies[21]. Although aptamers are selected for target binding *in vitro*, they are also capable of binding to their targets *in vivo* with good affinity and, as a result, many aptamers have been utilized for drug delivery and even as drugs themselves[22]. Aptamers are also easy to modify chemically, which allows for different methods of attachment onto supportive matrices. In most types of sensor systems, the support matrix plays a large role in signal transduction; therefore the immobilization chemistry can have a significant effect on the sensitivity and selectivity of the sensor[23]. For the purpose of electrochemical detection, the support is typically a solid electrode, commonly gold, although other electrode materials, such as glassy carbon and indium-tin oxide (ITO), are also used[23].

Like antibodies, aptamers have the ability to bind to unique epitopes of protein targets via sequence specific hydrogen-bonding between the bases and amino acid side-chains[24]. Similarly, the importance of higher order structures to protein binding affinity and specificity is mirrored in the importance of secondary structures to aptamer binding[25,26]. This has important implications for the choice of aptamer building blocks. DNA normally found in living cells are in double-strands and thus unlikely to form the complex secondary structures required for target binding. However, DNA is more stable than ribose nucleic acid (RNA) due to the lack of 2’-OH on the ribose ring[5], and therefore

generates aptamers that are more stable for practical applications. The solution to this dilemma came when Ellington, et al demonstrated that modifications to the original aptamer selection protocol can produce single-stranded DNA aptamers[27]; this helped propel aptamers into the forefront of sensor research. Since that time, many different variations and improvements of the selection protocol has been published[28-31]; of special interest is the research by Ruff, et al for generating *in vitro* selection libraries that enhance secondary structures of DNA aptamers[30].

1.4. *In vitro* selection of aptamers

Aptamers are generated via an *in vitro* selection method commonly known as SELEX (systematic evolution of ligands by exponential enrichment)[10,11]. As mentioned above, various modifications to the original SELEX procedure have been reported, such as capillary electrophoresis SELEX[32], atomic force microscopy SELEX[31], and automated SELEX[28]. More comprehensive reviews on the many types of *in vitro* selection can be found elsewhere[33-35]; a general description of the conventional SELEX method that is commonly employed in most academic laboratories will be given below.

The selection process begins with the solid phase synthesis of a library of random oligonucleotides, either single-stranded RNA or single-stranded DNA that is approximately 40 – 80 nucleotides long containing between 10^{13}- 10^{15} different sequences [33]. Due to the importance of secondary structures to target binding, libraries containing alternating regions of purine and pyrimidine designed to increase the probability of generating stem-loop structures have been proposed[30]. The random oligo region is flanked with two primer regions, usually between 15 – 18 nucleotides in length, that allows for the polymer chain reaction (PCR) amplification of the successful target binding sequence in the subsequent steps; for an RNA sequence it will be necessary to first transcribe the RNA into the equivalent DNA sequence prior to amplification.

In the conventional SELEX method, the target is affixed onto a solid support, typically silica gel in a column, via biotin-streptavidin interactions[35]. The library is then

incubated in the column to allow the binding sequences to interact with the target. The column is then washed with buffer in order to separate out the non-binding sequences. The binding sequences are then eluted out from the column under highly chaotropic conditions (i.e. strongly denaturing environment) and then amplified using PCR. The successful sequences are then returned to the column and another iteration of the cycle begins (Figure 1-4). Usually 10 to 20 cycles are enough to generate aptamers with consensus sequences[17]. The incubation times in the selection column are typically on the order of a few minutes but if an aptamer with faster binding kinetics is desired then the incubation time can be decreased during the last few rounds in order to place an increased selection pressure on the library. Sometimes counter-selection is performed using a secondary target with a similar structure so as to ensure that the successful aptamer is selective only for the desired target. In counter-selection, alternating cycles are carried out where sequences that bind to the secondary target are removed from the selection pool. Sequence minimization is then performed to determine the smallest possible binding sequence. This entails reducing the aptamer, typically starting with the primer regions, until the binding affinity of the aptamer for its target becomes significantly reduced. In this way, it is possible to locate the vital regions of the aptamer and potentially elucidate the secondary structure of the binding region.

Figure 1-4: General schematic of the conventional SELEX process.

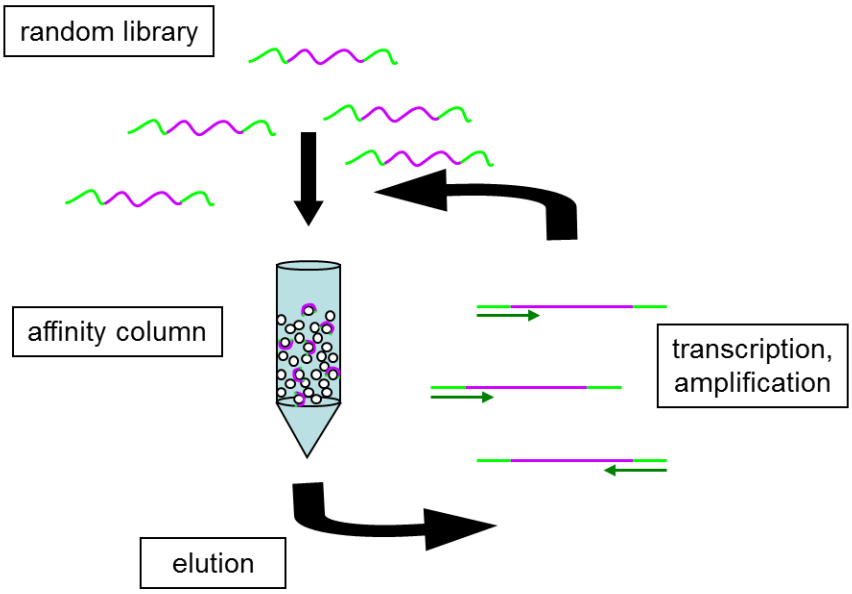

A library consisting of random sequences of 40 – 80 nucleotides (in purple) flanked by PCR primer regions (in green) is introduced into an affinity column. The immobilized target is used to capture aptamer candidates which are later eluted for PCR amplification prior to reintroduction to the affinity column for the next cycle.

One of the major limitations with *in vitro* selection is that optimal binding will usually occur only under the selection conditions (so-called “selection pressures”). These can strongly affect resulting attributes of the aptamer and, as a result, the selection conditions typically emulate physiological environments. The versatility of the SELEX protocol for selecting aptamers that target a wide range of biologically relevant molecules is a large part of the appeal of using aptamers as the sensing element in biosensors.

1.5. Immobilization of DNA on gold electrodes

The first step to creating an aptamer-based sensor is the immobilization of the aptamers onto a solid support surface; for electrochemical aptamer-based sensors, the preferred conductive support is gold. Since aptamers are comprised of DNA or RNA,

the vast amount of research reported for electrochemical DNA hybridization sensors will also apply. A general approach to immobilize aptamers onto gold is to modify the single-stranded DNA at the 5'-end with an alkanethiol linker, which binds onto gold via robust Au-S interactions and self assembles into a monolayer on the surface. It is also possible to modify the 3'-end of the oligonucleotides with alkanethiol to immobilize onto gold; however, Barton's group has shown that DNA duplex immobilized through the 3'-end will lie flat on the electrode surface[36], thus impeding interactions with solution-based targets; whereas those immobilized through the 5'-end do not have this issue as they protrude away from the surface at 45° from normal[37] (Figure 1-5). It was suggested that this difference may arise from the placement of the alkyl chain within the major groove of the duplex structure in the 3' thiolated DNA[36]. The 3'-end of the 5'-immobilized DNA is typically modified with a small molecule redox marker in order to signal the occurrence of a binding event.

Figure 1-5: Orientation of 5'- and 3'-end immobilized DNA on gold electrodes.

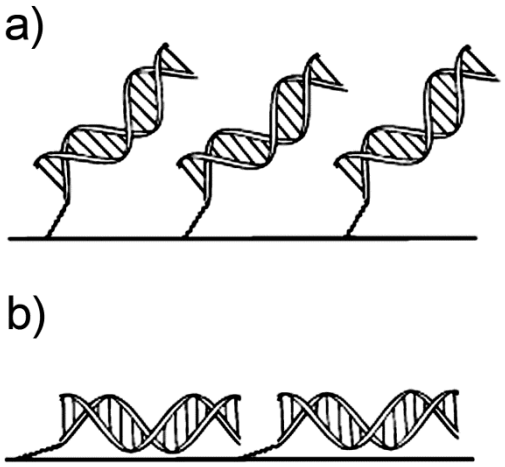

a) The orientation of 5'-end immobilized DNA protrudes from the surface at 45° from normal. b) The orientation of 3'-end immobilized DNA lies close to the surface. Adapted with permission from [37]. Copyright (1998) American Chemical Society.

Herne and Tarlov also noted a non-specific absorption issue, i.e., the aromatic purine and pyrimidine bases also strongly absorb to gold surfaces[38]. The use of alkanethiol alcohol to form mixed monolayers with alkanethiol-DNA created modified

gold electrodes with significantly better electrochemical response compared to monolayers comprised purely of alkanethiol-DNA (Figure 1-6)[39]. The use of longer alkanethiols to passivate DNA-modified gold electrode surfaces has been found to give electrodes that are more orderly and more stable towards long-term dry storage[40], however, shorter alkanethiol monolayers have better electron transfer properties[40,41]; six carbon alkanethiol (mercaptohexanol or MCH) is currently the most common alkanethiol alcohol used to treat DNA-modified surfaces[41] due to its optimal passivation properties.

Figure 1-6: Comparison of cyclic voltammograms of surface passivated and non-passivated electrodes

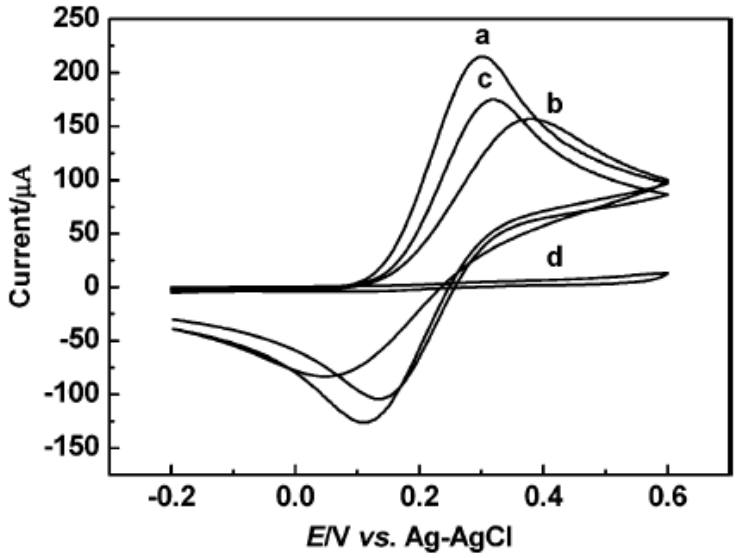

Cyclic voltammogram of 20.0 mM $[Fe(CN)_6]^{4-/3-}$ probe in 10 mM 4-(2-hydroxyethyl)-1-piperazineethanesulfonic acid (HEPES) buffer solution (pH 8.0) at scan rate of 100 mV/s for (a) bare gold electrode, (b) thrombin binding aptamer modified electrode, (c) thrombin binding aptamer/mercaptoethanol functionalized electrode, and (d) after formation of aptamer thrombin complex at the surface of the thrombin binding aptamer/mercaptoethanol functionalized electrode with 15.0 nM thrombin solution for 10 min. Reprinted with permission from [39]. Copyright (2005) American Chemical Society.

Other features of self-assembled monolayers of DNA on gold, such as surface coverage and length of the alkyl chain, have significant effects on DNA hybridization efficiency with solution-diffused complementary strands[38,42-45]. Modifications to the basic DNA immobilization protocol, either by using lower concentrations of DNA[41] or by limiting

the immobilization time[46], has no significant effect on the resulting electrode properties aside from surface density; however, the surface density of DNA-modified electrodes determines many of its properties[46]. Electrodes with high DNA surface density have lower hybridization efficiency compared with electrodes of lower density due to increased steric hindrance[46]. However, if the surface density is too low, then the hybridized DNA probe will flex towards the surface and the electrochemical sensor will be unable to distinguish between hybridized and un-hybridized probes[47]. Optimal surface density for hybridization is best achieved by the immobilization of duplex DNA that is then dehybridized, leaving behind a single-stranded DNA surface that has plenty of room for a complementary strand to bind[48]. The effect of surface density on aptamer-based electrochemical sensor response and kinetics have not been extensively studied, however, White et al. [41] and Cheng et al. [49] have found that their electrochemical sensors for cocaine and lysozyme, respectively, perform better at significantly lower surface densities.

1.6. DNA charge transfer

It has been suggested by Barton's research group that charge transfer in DNA occurs through the π-stacking of the aromatic bases[50-54]. Long-range electron transfer was found to proceed through hole migration[53] from the guanine residues to the charge acceptor through the base-stacked bases[55]. The nature of the charge donor or acceptor and its integration into the base-pair stacking of the DNA has been found to be critical to the charge transfer in solution and on surfaces[50,56]. Charge transfer through the bases over a distance of 10 base-pairs[57] and even 100 base-pairs[58] has been demonstrated.

Another possible model of DNA charge transfer that applies to DNA-modified electrode surfaces has also been reported[59,60]. It is proposed that the formation of double-stranded DNA induce changes in DNA flexibility, which, in turn, modifies the electron transfer process between the electrochemically active redox marker attached onto the DNA and the electrode[60-62]. Anne and Demaille have demonstrated that for short 20-mer double-stranded DNAs (dsDNAs) it is possible to model it as a rigid rod

attached onto a flexible elastic linker[60] and the thermal motion of the immobilized dsDNA depends heavily on the length and flexibility of the alkyl linker[61].

1.7. Aptamer-based electrochemical sensors

It is possible to classify electrochemical biosensors into two broad categories based on the nature of the target recognition mechanism, which can then be divided into more specific subcategories. Labeling methods require the use of a redox active compound, attached either to the aptamer probe or the analyte itself, to signal a molecular recognition event; these include the dual binding site-based detection schemes and the conformational change-based detection schemes. Label-free methods, on the other hand, detect binding events through a change in the physical or chemical properties of the electrode itself, with or without the use of a redox marker in solution. These include the conductivity change-based detection scheme and the surface property-based detection schemes. The main advantage of label-free methods is that they tend to be less complex than labeled systems. It is important to note that the majority of aptamer-based electrochemical sensors are created with DNA-based aptamers. Although RNA aptamers can have more complex secondary structures compared to DNA aptamers, the resulting improvement in binding ability is off-set by their instability toward hydrolysis due to the hydroxyl group on its 2' carbon[5]. DNA-based aptamers are more stable and as a result, they are more amenable to sensor applications.

1.7.1. Dual binding site-based detection schemes

The basic construction of the dual binding site-based electrochemical sensor uses the same concept as an enzyme-link immunosorbent assay (ELISA) which relies on the availability of two binding sites on the same analyte. In this detection scheme, an unlabelled aptamer (probe aptamer) is first immobilized onto the electrode substrate then the target is allowed to bind (Figure 1-7). After that, a second redox labelled aptamer (signalling aptamer) is bound onto the target allowing for electrochemical

detection. The final construct resembles a sandwich and is often referred to as the "sandwich"-type detection scheme.

There are two common types of labels for dual binding site based electrochemical sensors; enzymatic labels catalyze redox reactions whereas small molecule labels are directly involved in the electrochemical reaction. In enzyme labelled sensor systems, enzymes are typically cross-linked to streptavidin or avidin and then allowed to interact with the biotinylated aptamer to form the aptamer-enzyme conjugate for signalling. The aptamers are typically covalently bound to biotin via standard phosphoramidite chemistry[63] and are commercially available[64,65]; alternatively, it is also possible to attach biotin to the aptamers via the use of biotinylated primers in the PCR amplification step. Small molecule redox labels can be covalently tethered to the 5' or 3' end of the aptamer strand or they can be non-covalently bonded via base intercalation or via charge interactions[66]. It is also possible to modify signalling aptamers with quantum dots and nanoparticles, in place of enzymes or small molecules, which will either catalyze a redox reaction[67] or be dissolved and quantified in subsequent electrochemical measurements[68,69].

Figure 1-7: The general scheme of the dual binding site-based detection strategy to create aptamer-based electrochemical biosensors.

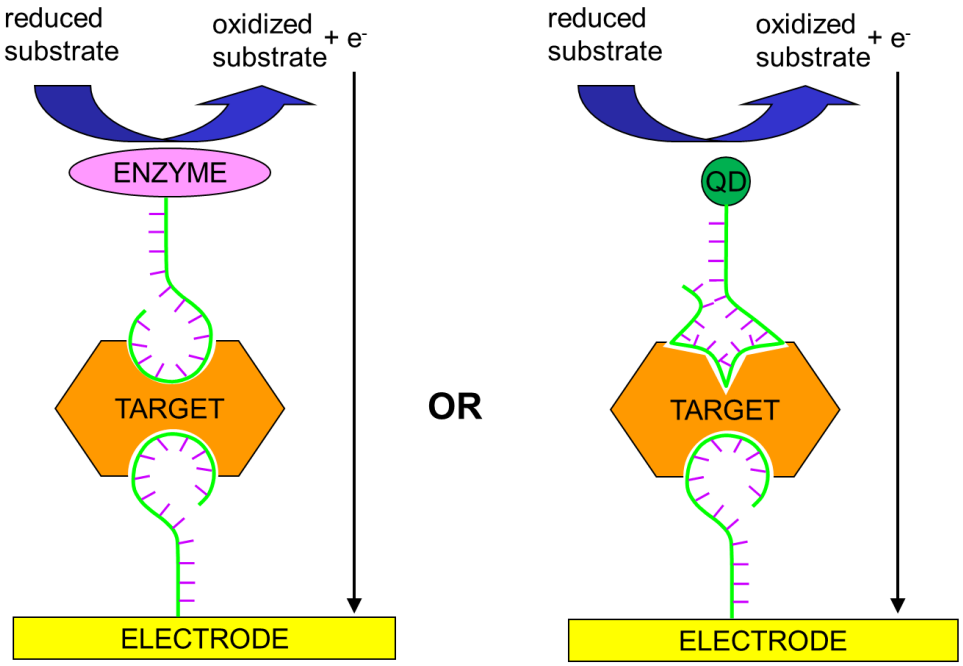

For targets with more than one binding site for a particular aptamer (left) it is possible to modify the aptamer with an enzyme or a quantum dot and use it as part of the electrochemical signaling mechanism. For targets with only one binding site for a particular aptamer (right), the selection of a second aptamer that binds on another region of the target is required.

For the dual binding site-based detection scheme to work there must either be multiple binding sites on the target protein available for the same aptamer or there must be two different signalling and probe aptamers binding at different sites. A dual binding site-based sensor design using enzymatic redox markers with two different thrombin binding aptamers has been demonstrated by Ikebukuro et al. [70]. The thiolated 29-nuclecotide aptamer (probe) was immobilized onto a gold electrode while the 15-nucleotide aptamer (signalling) was modified with biotin, and then coupled to an avidin-modified glucose dehydrogenase (GDH)[71]. After introducing thrombin onto the sensor, the GDH-modified signalling aptamers was allowed to bind onto the thrombin. Coulometry was performed to quantify the thrombin in a glucose containing buffer spiked with a charge carrier, 1-methoxyphenazine methosulphate (m-PMS), to facilitate charge transfer between the enzyme and the electrode. The limit of detection for this sensor

was 1 μM[70], a few orders of magnitude higher than the reported nanomolar binding affinity of the thrombin binding aptamers[72]. Ikebukuro et al. proposed that this was a result of the low activity of the enzymatic label and so they redesigned their thrombin sensor with a new catalytic enzyme and exchanged the positions of the 15 nt and 29 nt aptamers in the sensor system. Pyrroquinoline quinone glucose dehydrogenase (PQQ - GDH) conjugate was chosen as the new enzyme[73] due to its high activity and its insensitivity to oxygen which is a major advantage for its use in a biological sample[74] (Figure 1-8a). They found that this new enzyme improved the limit of detection of the thrombin sensor by two orders of magnitude (10 nM) and gave a linear response to thrombin between 40 to 100 nM[73] (Figure 1-8b).

Figure 1-8: Sandwich-type detection based thrombin sensor

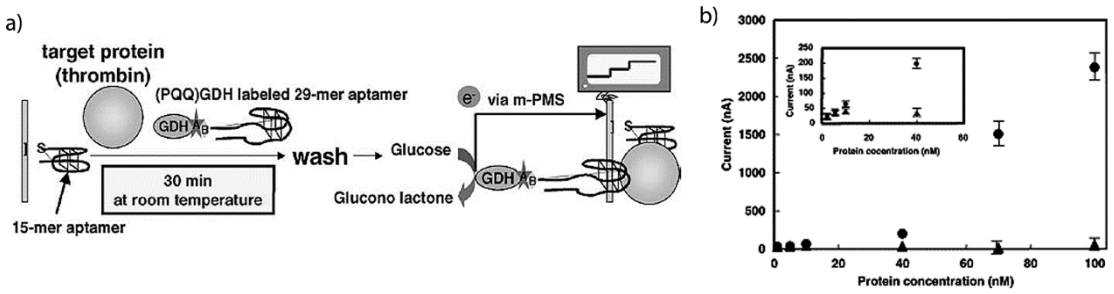

a) Detection scheme of the dual binding site-based electrochemical thrombin sensor using a pyrroquinoline quinone glucose dehydrogenase [(PQQ)GDH] enzymatic label. b) Concentration dependent sensor response with thrombin (circles) and negative control, BSA (triangles). Insert: magnified plot between 0 to 60 nM thrombin. Figures adapted from reference [73].

If the target protein only has one aptamer binding site, it is possible to use a labelled antibody that binds at a different site on the target as the signalling beacon. This was the detection scheme implemented by Centi et al. in their c-reactive protein (CRP) sensor[75]. CRP is a known serum biomarker for systematic inflammation and has been implicated in many chronic illnesses, such as diabetes, cancers, Alzheimer's, and cardiovascular diseases[76]. In order to overcome the instability of RNA in biological fluids, Centi et al. modified the RNA-based CRP-binding aptamer with fluorinated pyrimidines and immobilized it onto streptavidin coated magnetic beads[75] (Figure 1-9). After binding to CRP, the magnetic beads were washed and incubated with biotinylated

IgG-anti-CRP antibodies. The signalling enzyme, alkaline phosphatase (ALP), was cross-linked to streptavidin and allowed to interact with the biotinylated IgG-anti-CRP antibodies. The sensor was exposed to different concentrations of CRP in the presence of the enzymatic substrate, α-naphthyl phosphate (which is hydrolyzed into 1-naphthol by ALP). Differential pulse voltammetry (DPV) was performed above a magnetic block which attracted the magnetic bead immobilized aptamer-target-enzyme construct towards an electrode surface. One of the major advantages of immobilizing the aptamer onto a magnetic bead versus a solid electrode is that the bead can be suspended in a biological sample and is thus less dependent on target diffusion for aptamer and enzyme binding to occur which will reduce time needed to reach equilibrium.

Figure 1-9: C-reactive protein sensor using modified magnetic beads

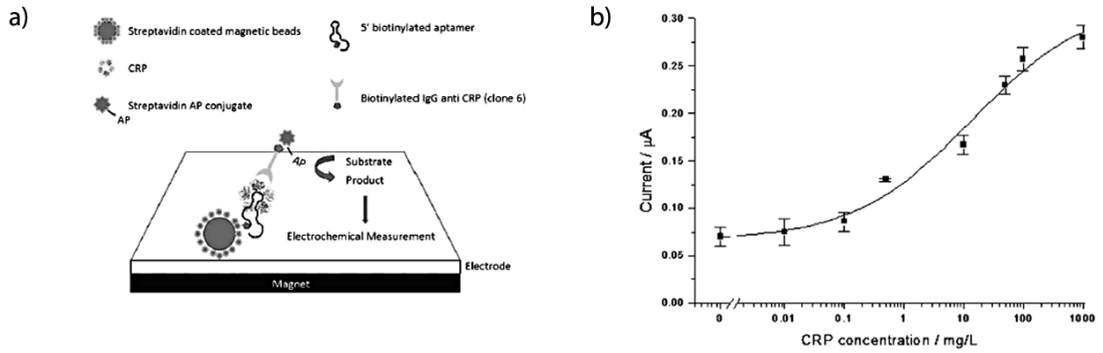

a) Schematic of c-reactive protein sensor using streptavidin-coated magnetic beads and anti-CRP antibody. Prior to the detection of the enzymatic product, the magnetic beads were concentrated onto a magnet-backed electrode. b) Dose-response curve of the sensor for CRP in 10x diluted serum. Solid line: theoretical sigmoidal data interpolation. Copyright Wiley-VCH Verlag GmbH & Co. KGaA. Reproduced with permission from reference [75].

Although the majority of aptamer-modified electrodes tend to use gold as the electrode material, it is also possible to use other electrode materials. As an alternative to gold, Xiang et al. designed a thrombin sensor using an aptamer-modified glassy carbon electrode[3]. The 15 nt, amine-modified anti-thrombin aptamer was immobilized onto the glassy carbon electrode following the electrochemical polymerization of *p*-amino-benzoic acid on the surface. The 29 nt, amine-modified thrombin binding aptamer was covalently linked to a single-walled carbon nanotube (SWCNT) that had

been treated with ALP. The ability of the SWCNT to bind multiple enzymes allowed it to act as a redox signal amplifier. During cyclic voltammetry in the presence of the substrate, *p*-aminophenylphosphate (*p*-APP), it was shown that this sensor has a limit of detection of 10 ng/mL, corresponding to a concentration of about 277 pM[3]. In order to improve the detection limit, Xiang et al. introduced redox recycling to this sensor with the addition of a secondary enzyme, diaphorase (DI). The product of the *p*-APP dephosphorylation by ALP, *p*-aminophenol (*p*-AP), is electrochemically oxidized to *p*-quinonimine (*p*-QI) on the surface of the SWCNT. In the presence of DI, *p*-QI is then reduced back into *p*-AP which can then be cycled back into *p*-QI again. The DI is then regenerated by the addition of NADH in the system (Figure 1-10). The limit of detection of this sensor is 0.3 pg/mL, corresponding to a concentration of 8.3 fM. This is a significant improvement over the single enzyme signalling sensor.

Figure 1-10: Ultrasensitive thrombin sensor with redox signal amplification

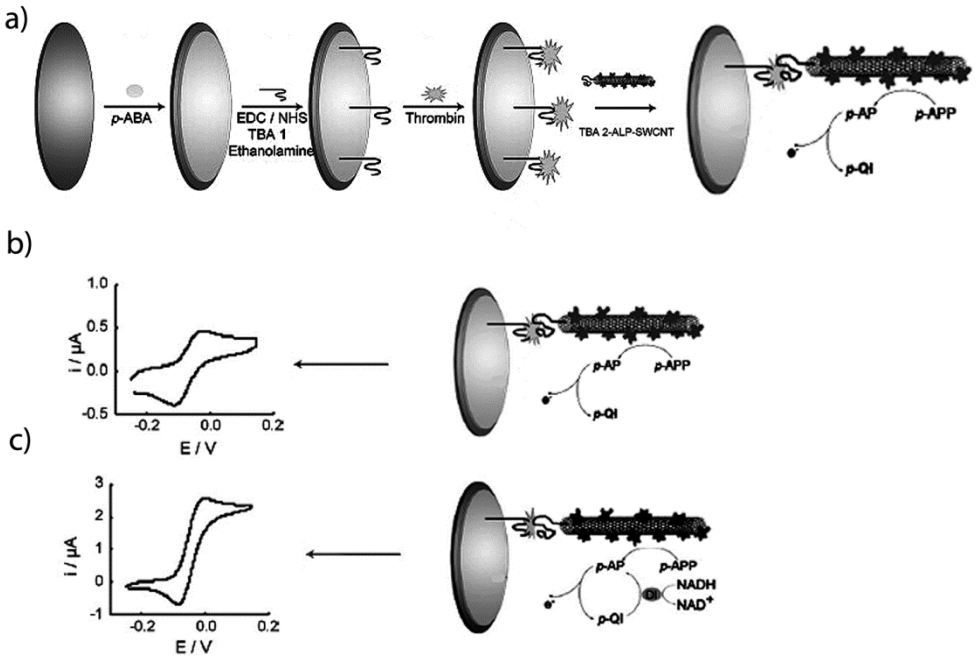

a) Schematic for the fabrication of a thrombin sensor using alkaline phosphatase-modified single-walled carbon nanotube. The current signal (peak current in cyclic voltammograms (left)) increases by about three orders of magnitude in the redox cycling enzymatic sandwich-type design (c) compared the normal enzymatic sandwich-type design (b). Reprinted from *Biosens. Bioelectron.* 25, Xiang, et al. "Ultrasensitive aptamer-based protein detection via a dual amplified biocatalytic strategy", 2539-2542, copyright (2010), with permission from Elsevier.

1.7.2. Conformational change-based detection schemes

Another common electrochemical detection scheme is the conformational change-based design, where target binding induces a transformation in the three dimensional structure of the aptamer, or aptamer assembly structure. This in turn results in an alteration in the electrochemical response of the sensor.

1.7.2.1. Aptamer structure change-based detection schemes

Figure 1-11: Diagrams of electrochemical aptamer sensors using the conformational change-based detection scheme.

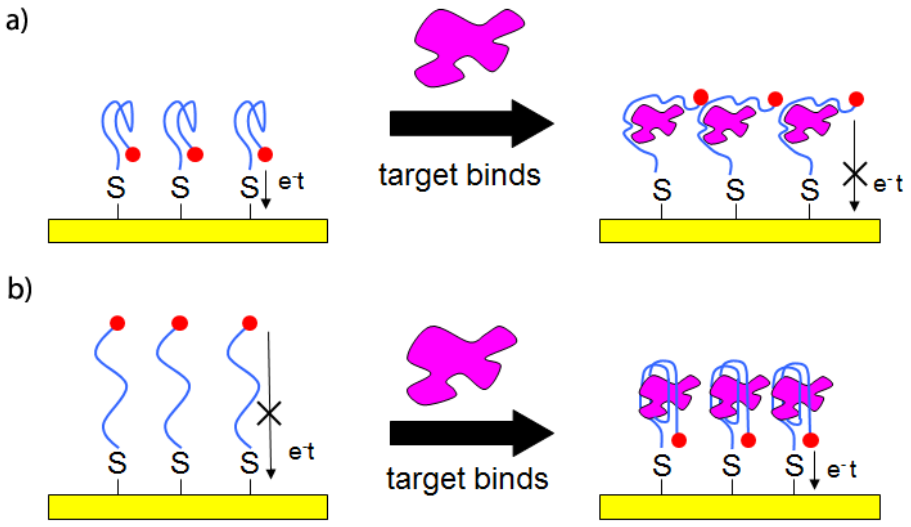

There are two possible modes of conformational change. a) illustrates the aptamer unfolding mode. Upon binding to the target, the aptamer sensor unfolds causing a disruption to the electron transfer between the end-labeled redox marker and the electrode surface. b) illustrates the aptamer folding mode. Upon binding to the target, the aptamer sensor folds up, bringing the redox marker close to the electrode surface and allowing electron transfer to occur.

In these types of sensors, the aptamers are typically end-labelled with a small molecule redox marker. Upon target binding, the aptamer can either fold into a more compact structure, thus bringing the redox marker closer to the electrode surface and increasing the rate of electron transfer and electrochemical signal, or the aptamer can unfold, thus moving the redox marker away from the electrode surface and decreasing the electrochemical signal (Figure 1-11). It is important to first fold the aptamer into the

appropriate secondary structure, which is typically the most thermodynamically favourable structure, prior to immobilization onto the electrode. This is usually done via the melting and slow cooling of the aptamer in the presence of the immobilization buffer which normally contains physiological salts at physiological pH.

The thrombin binding aptamer is known to fold into a compact G-quartet structure upon binding to thrombin[72,77,78]. Radi et al. took advantage of this feature by designing an electrochemical sensor for thrombin using the 15-nucleotide thrombin binding aptamer that has been modified on the 5' and 3' end with a thiol and a ferrocene group, respectively[79]. The aptamer was immobilized via the 5'-thiol onto a gold electrode that was then passivated with 2-mercaptoethanol, forming a mixed monolayer. Because of the short length of the aptamer, Radi et al. suggests that the folding of the aptamer upon thrombin binding will bring the 3'-ferrocene moiety to the electrode surface, thus increasing the electron transfer rate (Figure 1-12). Since the thrombin binding aptamer will also spontaneously fold into the G-quartet structure in the presence of high salt concentrations[80], Radi et al. examined the effect of different monovalent cations on the folding of the immobilized thrombin binding aptamer with fluorescence spectroscopy[79]. While the effect of Li^+ or Na^+ ions on the folding of the aptamer was significantly less than that of K^+, it was determined that the binding experiments in the absence of any salt showed the highest sensitivity. The sensor was then characterized by Radi et al. [79] using cyclic voltammetry (CV), differential pulse voltammetry (DPV), electrochemical impedance spectroscopy (EIS), and by Sánchez et al. [81] using chronoamperometry (CA), chronopotentiometry (CP) and square-wave voltammetry (SWV). It was demonstrated that this sensor has a limit of detection of 0.1 nM using SWV. It was also possible to regenerate the sensor up to 25 times by placing it in a stirred solution of 0.1 M hydrochloric acid for 60 seconds[81], making this sensor an appealing prospect for practical applications.

Figure 1-12: Conformational change-based thrombin sensor using the short thrombin aptamer

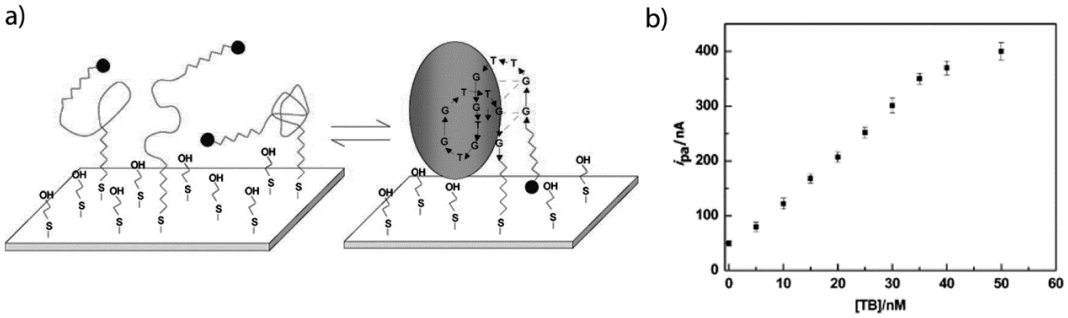

a) Schematic of an electrochemical thrombin sensor using the conformational change-based detection scheme. Target binding folds the aptamer into a G-quartet structure, bringing the ferrocene redox marker close to the electrode surface. Closed black circles represent the ferrocene moiety. b) Calibration curve of the sensor. Reprinted with permission from [79]. Copyright (2006) American Chemical Society.

Xiao et al. have also created a thrombin sensor with a small molecule redox marker[82]. They used the 32 nucleotide thrombin binding aptamer that had been 3'-end labelled with the redox marker methylene blue (MB). This sensor has been demonstrated to be able to detect the presence of thrombin even in complex biological matrices. In contrast to the thrombin sensor of Radi et al. [79], this sensor was created with a longer thrombin binding aptamer and, as a result, the electrochemical signal does not increase but rather decrease with increasing concentrations of thrombin. Xiao et al. proposed that this is due to the fact that the longer aptamer (a single-stranded DNA) is more flexible which allows random thermodynamic motion to bring the redox marker towards the electrode (Figure 1-13a). This increases the probability of the redox marker colliding with the electrode prior to binding to thrombin; after binding the aptamer folds into a G-quartet structure and is no longer as flexible. As a result the electrochemical signal decreases. Because the ionic strength of the environment correlated to the degree to which the thrombin binding aptamer folds into a G-quartet in the absence of its target, Xiao et al. tested the ability of their sensor to operate in buffers of different ionic strength[83]. As expected, they found that in high and medium ionic strength buffers, their sensor was less responsive to increased concentrations of thrombin, as a result of increased prevalence of G-quartets on the sensor surface prior to the introduction of

thrombin (Figure 1-13b). In addition to refining the electrochemical aptamer sensor architecture, it is also necessary to fine-tune the operating conditions in order to achieve optimal sensor sensitivity.

Figure 1-13: Conformational change-based thrombin sensor using the long thrombin aptamer

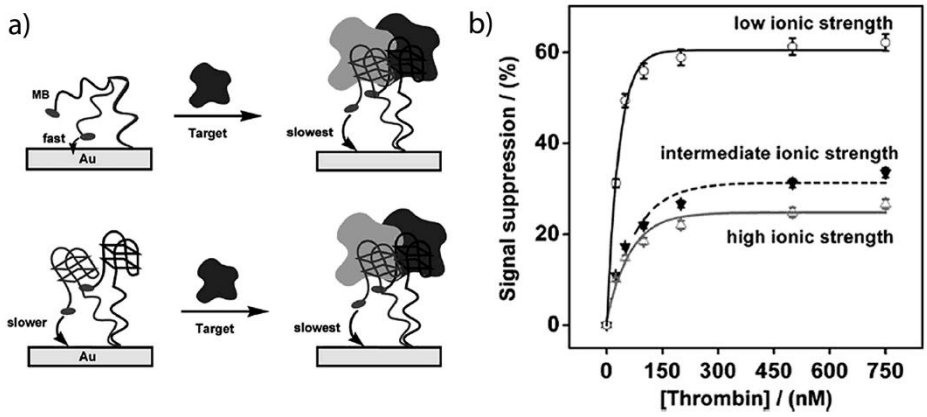

a) The two possible structures of a conformational changed-based sensor using the 32-base long thrombin binding aptamer. Top: the sensor in low ionic strength environment; bottom: in high ionic strength environment. b) Concentration dependence plots of the sensor under different ionic strengths [83]. Copyright Wiley-VCH Verlag GmbH & Co. KGaA. Reproduced with permission.

Like the thrombin-binding aptamer, the cocaine-binding aptamer is well-suited for incorporation into a conformational change-based architecture due to its binding dependent secondary structure. The cocaine-binding aptamer was first identified by Stojanovik et al. as a three-way junction with the cocaine binding site at the center[84] (Figure 1-14a). Despite being partially folded prior to the binding of cocaine, the aptamer is still flexible at one end; this flexibility allowed Baker et al. to create an electrochemical sensor to detect cocaine in a complex biological matrix[85]. Methylene blue (MB) was attached to the 3' end of the aptamer as a redox active electrochemical label. The aptamer is then partially folded and immobilized onto a gold electrode surface at the 5' end (Figure 1-14b). Upon binding to cocaine, the aptamer folds itself into a rigid three-way junction and brings the MB tag close to the electrode surface, increasing the electrochemical signal. This sensor was found to be unresponsive to common cocaine cutting agents such as flour and sugar while simultaneously being responsive to

cocaine. Swensen et al. then went on to create a real-time microfluidic electrochemical sensor for cocaine using the same electrode design[86]. This real-time sensor had a response time of less than one minute. After the sensor was saturated with cocaine, regeneration of the sensor can be done by flushing the system with cocaine-free solution.

Figure 1-14: Aptamer structure changed-based cocaine sensor

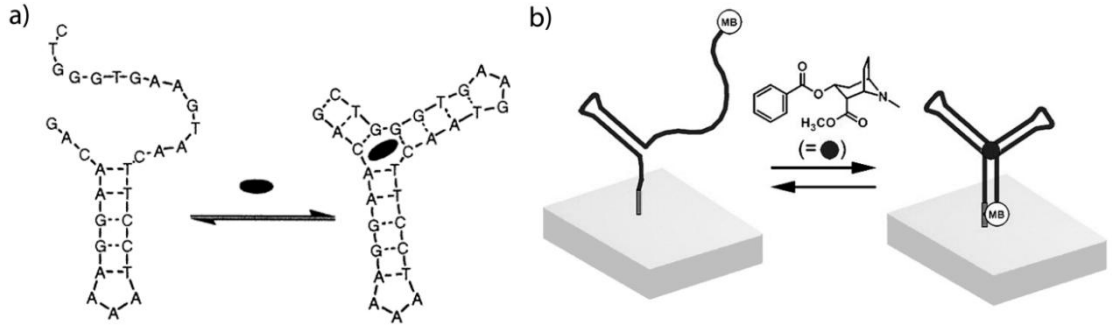

a) Structure of the cocaine-binding aptamer before and after binding its target. Reprinted with permission from [87]. Copyright (2001) American Chemical Society b) The detection schematic of the conformational change-based electrochemical cocaine sensor. MB = redox marker methylene blue. Reprinted with permission from [85]. Copyright (2006) American Chemical Society.

1.7.2.2. Aptamer assembly structure change detection schemes

Although using target binding induced aptamer conformational change to detect analytes is an elegant approach to the signal transduction task, it is not easily generalized because not all aptamers will fold into or unfold from a more compact form upon target binding. Another option would be to engineer aptamer-based nucleic acid assemblies that will mimic these types of binding activated structural changes.

The simplest design for these assemblies is to use a complementary nucleic acid to hybridize to a labelled aptamer immobilized onto the electrode surface. This produces a double-stranded nucleic acid that is much less flexible than a single-stranded aptamer and will protrude away from the electrode as a result, limiting electrode transfer from the end-tethered redox marker to the electrode. Upon adding the target analyte, competitive displacement of the complementary strand will cause the aptamer assembly to

dehybridize leaving only flexible single-stranded aptamers on the electrode surface, allowing faster electron transfer and increased electrochemical signal. Zuo et al. created an aptamer-based adenosine triphosphate (ATP) electrochemical sensor based on this design (Figure 1-15a)[88]. Their sensor had a limit of detection of 10 nM and was highly selective to ATP. This sensor was also capable of detecting ATP *in vitro* from a freshly lysed cell culture, demonstrating its selectivity and sensitivity in a complex sample matrix. Alternatively, it is also feasible to immobilize the labelled complementary strand on the electrode instead; such a strand should be designed so that it will fold into a hairpin structure after the displacement of the aptamer strand (as this will improve electrochemical signal at the sensor). Lu et al. created an ATP sensor with the anti-ATP binding aptamer, which had complementary bases on its 5' and 3' ends to allow hairpin folding (Figure 1-15b)[89]. They also created a thrombin sensor with the anti-thrombin aptamer, which does not have this feature, so the 3' end of the thrombin binding aptamer was extended with additional bases to create a complementary region for forming a hairpin[89]. However, the addition of Mg^{2+} to the target binding buffer was required after the removal of the aptamer strand from the electrode upon target binding in order to induce the Watson-Crick base pairing that forms the hairpin.

Figure 1-15: Complementary strand displacement based ATP sensor

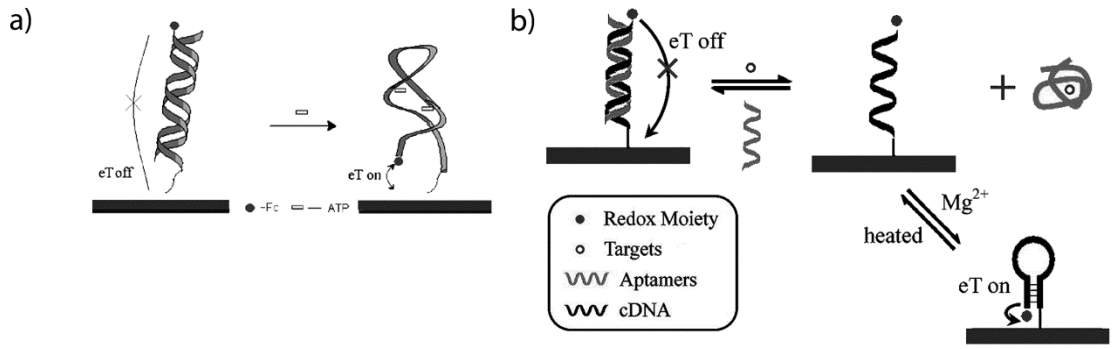

a) A simple aptamer-based assembly with complementary DNA that is displaced by the target for ATP detection. Reprinted with permission from [88]. Copyright (2007) American Chemical Society. b) A variation of a) where the complementary strand is immobilized onto the electrode instead and folds into a compact structure upon displacement of the aptamer due to target binding. Reprinted with permission from [89]. Copyright (2008) American Chemical Society.

1.7.3. Conductivity change-based detection schemes

Aside from forming binding-dependent sensor architecture, it is also possible to design an aptamer assembly that can moderate charge transfer through the base pairing of a ds-DNA to depend on the binding state of the aptamer[90]. In a perfectly matched DNA duplex, the aromatic rings of the nucleotide are stacked one on top of another. This allows charge transfer to occur through the base-stacking; however, if the base-stacking is interrupted due to base mismatches then that charge transfer cannot occur[54].

Although the design of DNA conductivity change-based detection schemes are most easily exploited in aptamers that have specific binding-induced structural changes, e.g. binding sites that forms bulges, such as that found in the double-stranded adenosine aptamer, this design can be universally applied, albeit with a bit more difficulty, as demonstrated by Huang et al. [91] in their thrombin sensor that was constructed from a three-way junction between the thrombin binding aptamer and a double helical DNA conduction path (Figure 1-16a). It was proposed that the binding of thrombin to the aptamer domain will cause the aptamer stem to fold tightly into a G-quartet,[77,78,92] allowing the three-way junction to close up and repairing the otherwise interrupted DNA conduction path and allow charge transfer between the redox marker and the electrode to take place[91]. Five different three-way junctions, each composed of a different combination of nucleotides, were examined for their charge transfer properties using polyacrylamide gel electrophoresis assays. Once the best three-way junction was selected, a ferrocene marker was used to label the aptamer assembly, which was then immobilized onto a gold electrode (Figure 1-16b). Square-wave voltammetry was performed on the electrodes both before and after thrombin binding. The limit of detection of this sensor was found to be 5 pM with a linear range between 5 and 150 pM; which was several orders of magnitude larger than the previously reported dissociation constant (K_d) of this aptamer[72]. However this sensor showed a marked decrease in the linear range within a serum matrix.

Figure 1-16: Conductivity change based adenosine sensor

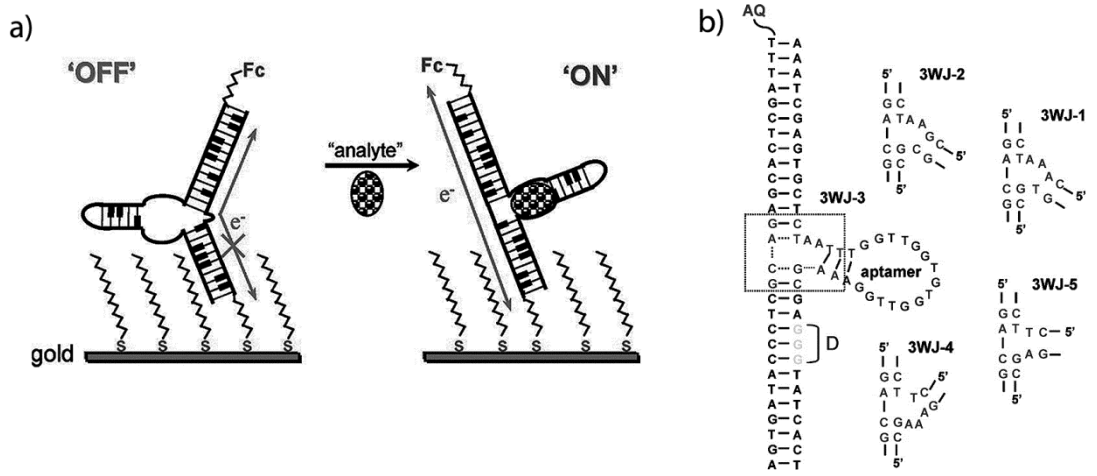

a) Upon binding to the analyte, the base-pairing of the signaling strand is reconstructed and electron transfer between the ferrocene redox marker and the electrode can occur. b) Rational design of the three-way junction between the thrombin binding aptamer and reporter stem. Five different junctions (3WJ-1 – 5) were examined; anthraquinone (AQ) was used as the electron donor for charge transfer to the triple G (D) in gel electrophoresis assays. Reprinted with permission from [91]. Copyright (2008) American Chemical Society.

1.7.4. Surface property change-based detection schemes

Aside from the above mentioned detection schemes, it is also possible to detect the binding of a target to an aptamer-based electrochemical sensor via a change of the surface property of the aptamer-modified electrode. While aptamer modified electrodes are negatively charged due to the phosphate backbone, the overall charge on the electrode surface can be altered upon the binding of a positively charged target. This will affect the diffusion of a charged solution based redox marker toward the electrode and influence the electrochemical responses of the electrode.

Rodriguez et al. first demonstrated this principal in their lysozyme sensor[93]. Lysozyme is a common antimicrobial enzyme that is positively charged at physiological pH. The single-stranded lysozyme binding aptamer was immobilized onto an indium tin oxide (ITO) electrode. Initially, the negatively charged oligonucleotide repelled the negatively charged $Fe(CN)_6^{3-/4-}$ redox markers in the physiological buffer solution and showed high charge-transfer resistance during electrochemical impedance spectroscopy

(EIS) measurements; however, upon binding to the positively charged lysozyme to the sensor, the resistance showed a marked decrease as a result of the increased overall charge at the electrode surface. The limit of detection of this sensor was 0.2 μg/mL[93].

Cheng et al. has utilized this same principal to create a lysozyme sensor with the positively charged redox marker, $Ru(NH_3)_6^{3+}$ (Figure 1-17a)[49]. However, by using a positively charged redox marker, the number of electrostatically bound redox markers decreases upon binding of lysozyme. This is a classic example of a "signal-off" sensor where increasing target concentration results in a decreased electrochemical signal. The limit of detection of this sensor was found to be 0.5 μg/mL, which is comparable to the sensor of Rodriguez et al.[93]. Cheng et al. also showed that there is an optimal surface density of aptamers that will give the best electrochemical response[49]. When the surface density is too high, the electrode response diminishes (Figure 1-17b). This is most likely due to the tightly packed aptamer strands on the surface causing steric hindrance that prevents lysozyme from binding. However, if the surface density is low, there are not enough aptamers on the surface to bind the target and the electrochemical response becomes weaker. It is important to note that this method of detection only works if the binding buffer is not at the pI of the protein target; otherwise the protein will have neutral overall charge and will not affect the charge density of the electrode surface.

Figure 1-17: Surface charge change-based lysozyme electrochemical sensor.

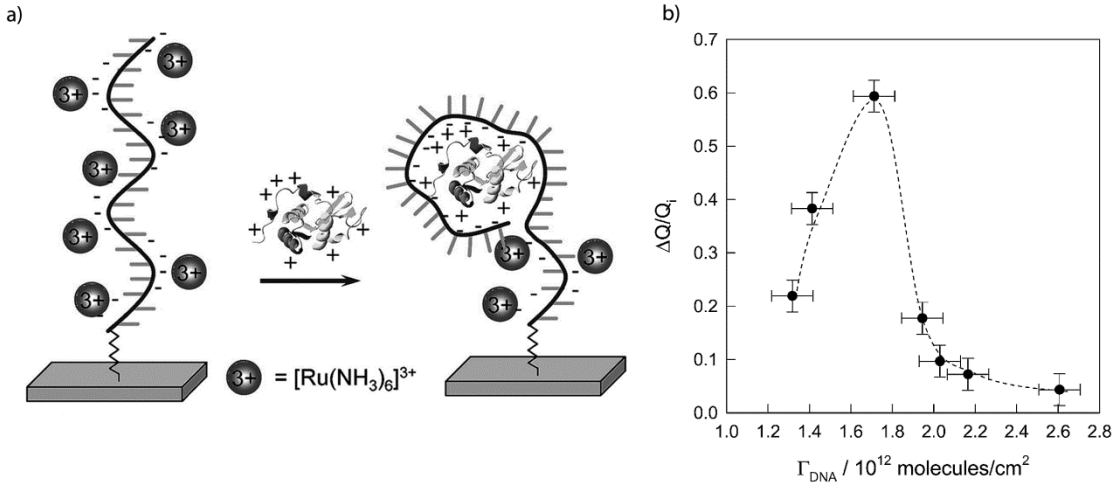

a) Change in charge density of the aptamer construct upon binding of the positively charged lysozyme target causes a dissociation of the charged $[Ru(NH_3)_6]^{3+}$ redox marker to the phosphate backbone. b) A plot of sensor response vs. surface coverage of aptamer at 10µg/mL lysozyme. The optimal surface coverage of aptamer on the surface of the electrode was found to be 1.7×10^{12} molecules/cm^2; at higher densities, the response of the electrode decreases. Reprinted with permission from [49]. Copyright (2007) American Chemical Society.

Another important effect of protein target binding to the surface of an electrode is that the surface itself is physically blocked off from the bulk of the buffer. As a result, electron transfer from the buffer will be limited. Cai et al.[94] and Radi et al.[39] reported the design of a thrombin sensor that took advantage of this effect independently. Cai et al. immobilized the 15 nt thrombin binding aptamer on a gold electrode that was then further modified with MCH to ensure the full passivation of the gold surface from the ferricyanide redox markers in the buffer (Figure 1-18)[94]. Despite surface passivation, the ferricyanide in the buffer can still be oxidized by the electrode. However, upon the binding of thrombin, ferricyanide is prevented from accessing the electrode and the rate of charge transfer slows. As a result, the charge transfer resistance, as measured by EIS, at the sensor surface increased. The limit of detection for this sensor was 0.1 nM[94]. Radi et al. also immobilized the 15-mer thrombin binding aptamer onto gold but protected the gold electrode surface with 2-mercaptoethanol instead of MCH[39]. While the limit of detection for this sensor was 2 nM[39], which is less than the sensor of Cai et al.[94], the sensor of

Radi et al. was shown to be capable of being regenerated and reused up to 15 times by treating the electrode surface with 2.0 M sodium chloride.

Figure 1-18: **Surface property change-based thrombin electrochemical sensor.**

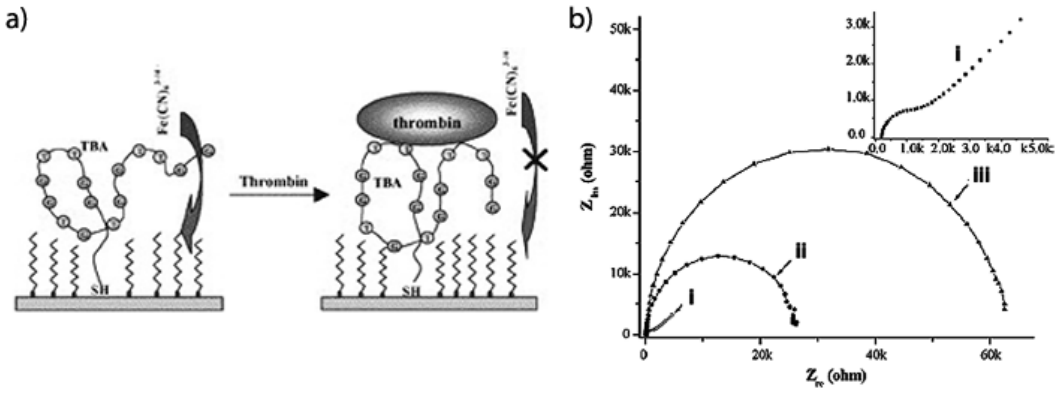

a) Upon binding of thrombin, the electroactive species $Fe(CN)_6^{3-/4-}$ is prevented from accessing the electrode surface. (TBA = thrombin binding aptamer.) b) Nyquist plots of i) the bare gold electrode, ii) TBA-modified gold electrode after surface passivation with mercaptohexanol and iii) the after 20 min incubation with a 1.0 μM thrombin containing buffer. Inset: magnified version of i). Radii of the semi-circular region of Nyquist plots are proportional to electrochemical impedance. Reprinted from *Sens. Actuators, B.* 114, Cai, et al. "Label-free protein recognition using an aptamer-based impedance measurement assay", 433-437, copyright (2006), with permission from Elsevier.

Zhang et al. used the same detection scheme in the design of a thrombin sensor with a polyamidoamine dendrimer to improve sensitivity[95]. A G_4-NH_2 polyamidoamine dendrimer was covalently linked to a gold electrode surface and then coupled to the thrombin binding aptamer to form a dendrimeric aptamer electrode which will have a dense surface concentration of the aptamers (Figure 1-19). Upon thrombin binding, the impedance at the electrode surface increases. The limit of detection of this sensor was 0.01 nM, a significant improvement on the thrombin sensors of Radi et al. and Cai et al. which were prepared on "normal" electrodes[39,94].

Figure 1-19: a) Schematic of the fabrication of a dendrimeric electrochemical thrombin sensor that uses the surface property change-based detection scheme.

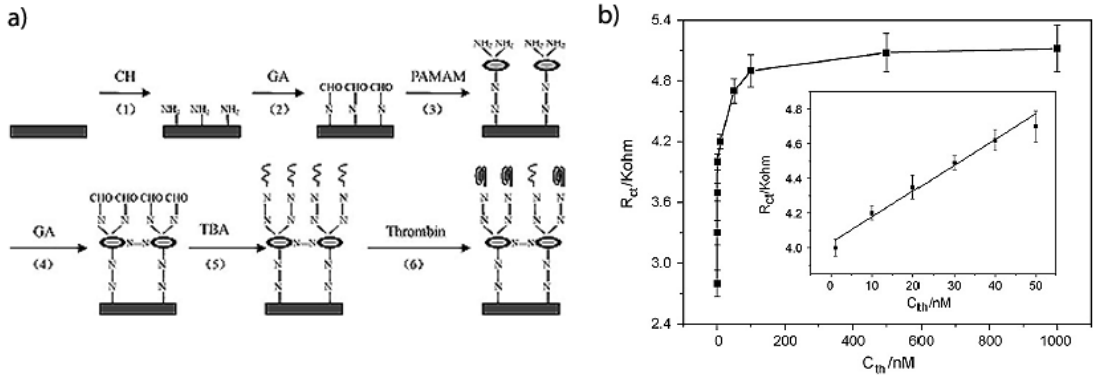

Upon binding to the thrombin target, the electrode surface is passivated and the conductivity of the sensor decreases. (CH = cysteamine hydrochloride, GA = glutaraldehyde, PAMAM = G4-amino-terminated polyamindoamine dendrimer, TBA = thrombin binding aptamer.) b) Electrochemical impedance spectroscopy (EIS) response (R_{ct} = resistance of charge transfer) of the dendrimeric electrochemical sensor at different concentrations of thrombin. Inset: Calibration curve of the EIS response. Reprinted from *Talanta.* 78, Zhang, et al. "A sensitive impedimetric thrombin aptasensor based on polyamidoamine dendrimer", 1240-1245, copyright (2009), with permission from Elsevier.

Aside from increasing surface density of the aptamer, there are other approaches to increasing target binding induced surface property changes. Protein target denaturation after binding on the electrode can significantly increase the surface area that is protected from the bulk buffer by unfolding the protein. Xu et al. created a modified target detection protocol by including a denaturing step with 6 M guanidine hydrochloride just prior to electrochemical measurements[24]. Their non-dendrimeric thrombin sensor had a limit of detection of 10 fM, which is several orders of magnitude better than the dendrimeric version of the same sensor. The combination of dendrimeric aptamers and target denaturation could potentially yield a sensor design with significantly increased sensitivity.

1.8. Objectives of this Thesis

Mucin-1 (MUC1) is a membrane-bound signalling oncoprotein associated with adenocarcinomas[96]. MUC1 localizes in the mitochondria and interacts with the tumour suppressor protein p53[97], thereby repressing the transcription of *p53* and stalling the p53-dependent apoptotic response to DNA damage[98]. Overexpression of aberrant MUC1 that is highly glycosylated is common in many forms of breast cancer[99]. In the extracellular domain of MUC1, there is a region called the variable tandem repeat region that contains a variable number of a highly conserved twenty amino acid sequence[96]. The VTR region is also the target of a commercial ELISA kit (CA 15-3) that uses two different monoclonal antibody, DF3 and 115D8.19.12, to detect the presence of MUC1 in the patient's bloodstream[100]. The dynamic range for detecting MUC1 with CA 15-3 is 5 U/mL - 250 U/mL,[101] which corresponds to approximately 0.8 μM - 39.7 μM[102].

In 2006, Missailidis et al. selected DNA aptamers that bind to the VTR region of MUC1[103]; of particular interest is the aptamer sequence MUC1 S2.2 which has a self-complementary region. Based on the results of *mfold* calculation, we propose that the 25-nt anti-MUC1 aptamer folds into a hairpin secondary structure in the absence of its target at room temperature (Figure 1-20). *mfold* is a computational software[104] written by Zukka that uses thermodynamic modelling to predict a minimum free energy (ΔG) for nucleotide secondary structures[105].

Figure 1-20: Two-dimensional structure of the 25-nt anti-MUC1 aptamer predicted using the mfold web server software[104].

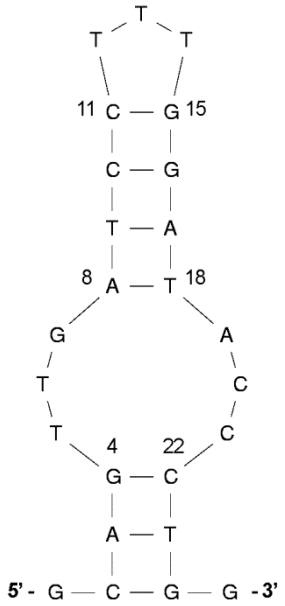

In this thesis, we propose to create an electrochemical aptamer-based sensor for MUC1, and to study the effect of surface density of immobilized hairpin DNA aptamers on sensor kinetics and electrochemical responses.

2. Electrophoretic mobility shift assay for confirming aptamer-analyte binding

It is important to be able to quantify the interaction between a newly selected aptamer and its target in order to ascertain the aptamer's suitability for use in its proposed application. For sensor applications, the aptamer's affinity for its target must be in the range of the target's biological concentrations. There are many methods that can be used to determine the binding constant (K_b), or its inverse, the dissociation constant (K_d) of an aptamer. Surface plasmon resonance[103], fluorescence resonance energy transfer (FRET)[102] and competitive ELISA assays[106] have been used to discover the dissociation constant of the 25 nt anti-MUC1 aptamer for the synthetic VTR MUC1 peptide, each presenting a different K_d. Electrophoretic mobility shift assays (EMSAs) are also known as gel shift assays and were used in this work in an attempt to determine the dissociation constant. EMSA was chosen because the previous methods used to determine the K_d all requires the immobilization of either the aptamer or the peptide onto a solid support, while EMSA is a solution-based method which will better reflect the dissociation constant that the anti-MUC1 aptamer has for its target *in vivo*. The EMSA of the anti-MUC1 proved to be difficult and in order to confirm that the issues were intrinsic to anti-MUC1 and not a result of technical difficulties, the gel shift of another aptamer with its target protein was performed.

2.1. Experimental

2.1.1. Reagents

Anti-MUC1 aptamer oligonucleotides (5'-GCA GTT GAT CCT TTG GAT ACC CTG G-3') and anti- connective tissue-activating peptide 3 (CTAP III) aptamer (seq. 27-1) (Thomas et al., in press) oligonucleotides (5'-CCA TGT TTT CTG GTA TTA TAC CAG CCG TTA CGC AAT CAT GG-3') were purchased from Integrated DNA Technologies, Inc. (Coralville, IA). The 40-mer 2×VTR MUC1 peptide (PDT RPA PGS TAP PAH GVT SA|P DTR PAP GST APP AHG VTS A) and 60-mer 3×VTR MUC1 peptide (PDT RPA PGS TAP PAH GVT SA|P DTR PAP GST APP AHG VTS A|PD TRP APG STA PPA HGV TSA) was purchased from Kinexus Bioinformatics Corp. (Vancouver, BC). OptiKinase was purchased from Affymetrix, Inc. (Santa Clara, CA). All other reagents were of reagent grade and used without further purification.

The unmodified anti-MUC1 aptamer was run on 15% denaturing polyacrylamide gels to confirm its size; the band of the correct size was excised from the gel and the oligonucleotides were extracted using the crush-and-soak method followed by ethanol precipitation[107]. The aptamer was then resuspended in TE buffer (10 mM Tris, 1 mM EDTA, pH 8).

Neutrophil-activating peptide 2 (NAP II) was a gift from Dr. Jason Thomas from the Microbiology and Biochemistry Department at Simon Fraser University. Briefly, the *in vivo* expression of the protein was as follows. The NAP II gene was inserted into the vector pET-21a and transformed into chemically competent *E. coli* BL21-de3 cells and expressed. The cellular extracts was purified with HPLC and desalted. The protein was then refolded in an oxidative buffer (2 M Guanidine-HCl/100 mM Tris-HCl (pH 8.6)/10 mM EDTA/2 mM oxidized glutathione/1 mM reduced glutathione) and cross-linked to form the appropriate biologically active quaternary structures. The protein was analysed by SDS-PAGE (Tris-tricine buffer system) with silver staining and ESI-MS[108].

The 2×VTR and 3×VTR MUC1 peptides were purified via HPLC with 0.1% v/v trifluoroacetic acid (TFA) in H_2O (A) and 0.1% v/v TFA in acetonitrile (B) co-eluting in a gradient from 100:0 to 60:40 A:B in 20 min. The mass of the peptides were confirmed with ESI-MS to be 3.754 kDa and 5.623 kDa for 2×VTR and 3×VTR respectively (Figure 2-1). The peptides were then dried and resuspended in phosphate buffered saline (137 mM NaCl, 10 mM Na_2HPO_4, 1.4 mM KH_2PO_4, 2.7 mM KCl, pH 7.4) and, due to the lack of strongly absorbing amino acids at 280 nm, quantification was done via UV absorption at 205 nm using the Scope's method[109].

2.1.2. Gel-shift assays

The anti-CTAP III aptamers were 5'-radiolabeled with (γ-^{32}P)ATP[110]. The reaction was then purified via denaturing polyacrylamide gel extraction[107]. Trace amounts (<1 nM) of (γ-^{32}P)ATP radiolabeled anti-MUC1 aptamers were folded by heating to 100 °C for 5 min and allowed to cool slowly to room temperature. The aptamer was then allowed to react with various concentrations of NAP II protein with 89 mM Tris, 25 mM KCl, 1 mM $MgCl_2$, pH 8 with 1 µg/mL poly(dI:dC) and 5% v/v glycerol for an hour at room temperature. Gel-shift assays were performed in 12% native polyacrylamide gels cast in 89 mM Tris, 25 mM KCl, 1mM $MgCl_2$, pH 8 buffer; the gels were run at 170 V and 4 °C for 45 min. The gels were exposed to a phosphor screen overnight at 4°C. The phosphor screens were scanned with a Typhoon 9410 Phosphorimager (*Molecular Dynamics*) and analyzed with the open-source image analysis software ImageJ (*http://rsbweb.nih.gov/ij/*).

Figure 2-1: Electrospray ionization – mass spectrograms of VTR peptides

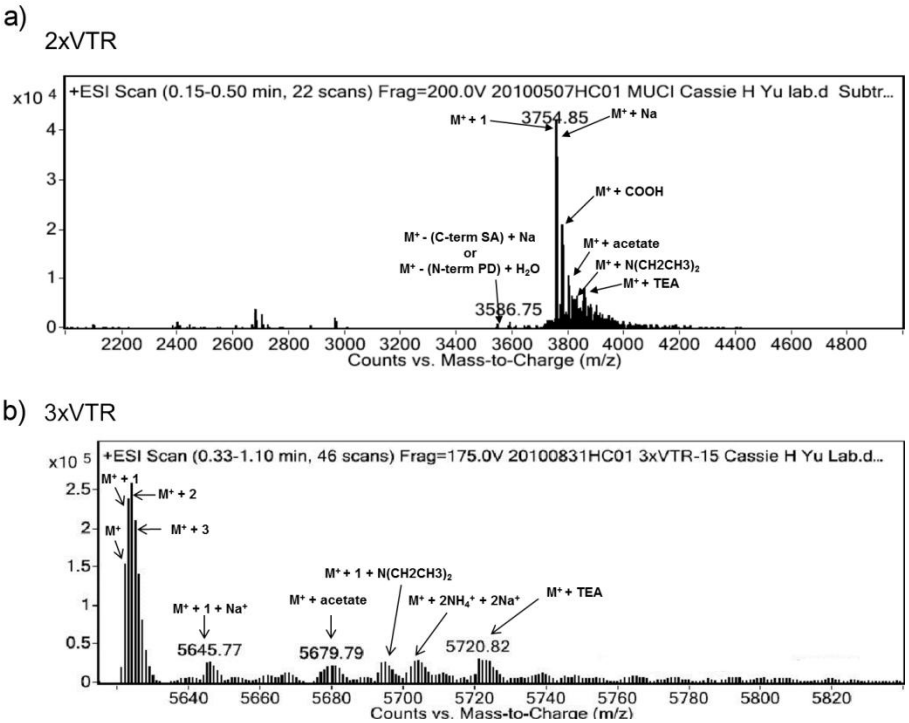

a) ESI-MS of the 2×VTR MUC1 peptide; theoretical mass was 3756.06 amu. b) ESI-MS of the 3×VTR MUC1 peptide; theoretical mass was 5625.0 amu.

The anti-MUC1 aptamers were 5'-radiolabeled with (γ-^{32}P)ATP[110]. The reaction was then purified via denaturing polyacrylamide gel extraction[107]. Trace amounts (<2 nM) of (γ-^{32}P)ATP radiolabeled anti-MUC1 aptamers were folded by heating to 100 °C for 5 min and allowed to cool slowly to room temperature or unfolded by heating as above and immediately cooled by liquid nitrogen. The sample was allowed to react with various concentrations of 3×VTR MUC1 or 2×VTR peptides in 100 mM Tris, 50 NaCl, 5 mM $MgCl_2$, pH 7.4 buffer (binding buffer 1) with 1 µg/ml poly(dI:dC) and 5% v/v glycerol. The reactions were equilibrated at room temperature overnight. Gel-shift assays were performed on 10% native polyacrylamide gels cast in 100 mM Tris, 50 mM NaCl, 5 mM $MgCl_2$, pH 8 buffer; the gels were run at 200 V and 4°C for 2 hours in the gel buffer. The

gels were then exposed to a phosphor screen overnight and scanned and analysed as described above.

2.2. Results and discussion

2.2.1. Gel-shift assay of anti-CTAP III aptamer

The EMSA of the anti-CTAP III aptamer was performed to analyze the binding between the recently selected aptamer (in press) and the expressed protein NAP II. The anti-CTAP III aptamer was selected by Thomas et al. using conventional SELEX techniques to bind to the multimeric CTAP III protein[108]. Both CTAP III and NAP II are the result of the different proteolytic cleavages of the platelet basic protein (PBP)[111] and the sequence of NAP II is truncated from the sequence of CTAP III[111]. A gel-shift assay had been performed on the anti-CTAP III aptamer with the CTAP III protein; however, a gel shift assay with the NAP II protein had not been performed.

The radiolabeled anti-CTAP III aptamer was folded by heating and slow cooling into secondary structures that might affect the binding affinity prior to the gel-shift assay. When the radiolabeled aptamer binds to the peptide, the electrophoretic mobility of the aptamer-peptide complex decreases due to its increased size and it travels slower through the polyacrylamide gel matrix compared to the aptamer on its own and causes the radioactive band in the gel to shift higher in position[112]. As the concentration of the peptide increases, a higher portion of the radiolabeled aptamer will be bound to the complex and the intensity of the shifted band will increase. A concentration dependence graph can be plotted in order to determine the equilibrium dissociation constant; the concentration of peptide at the point of 50:50 bound and unbound band intensity ratio is equal to the equilibrium dissociation constant (K_d)[113].

The gel shift assay of the anti-CTAP III aptamer with the NAP II protein showed a band shift at 2.5 nM NAP II (Figure 2-2a). Analysis of the band intensities gave a

concentration dependence plot (Figure 2-2b) corresponding to the equation describing the dissociation constant (Eq1)[113]. Using this equation, the K_d of the anti-CTAP III aptamer with the NAP II protein was extrapolated to be approximately 118 nM.

Figure 2-2: Gel shift assay of CTAP III

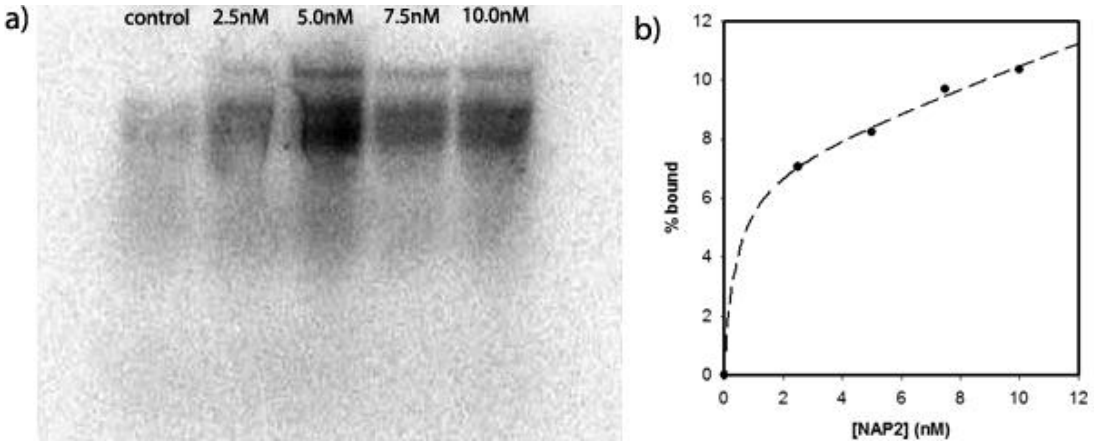

a) The EMSA of the anti-CTAP III aptamer with NAP II. The negative control lane (far left) shows multiple bands as a result of folding into multiple secondary structures. The 8% native polyacrylamide gel was cast and ran in buffer consisting of 89 mM Tris, 25 mM KCl and 1 mM $MgCl_2$ (pH ~8). b) Concentration dependence plot for the gel shift assay of the anti-CTAP III aptamer.

$$\%bound = \frac{[MUC1]_{eq}}{K_D + [MUC1]_{eq}} \quad \text{(Eq1)}$$

2.2.2. Gel-shift assay of anti-MUC1 aptamer

We propose that at room temperature the 25-nt anti-MUC1 aptamer, selected by Ferreira et al.[103], folds into a hairpin secondary structure. We first verified this hypothesis by using the *mfold* web server software (*http://www.bioinfo.rpi.edu/applications/mfold*) which uses thermodynamic modelling to predict the secondary structure of oligonucleotides[105] (both DNA and RNA) based on a set of prescribed conditions (100 mM NaCl, 5 mM $MgCl_2$, 25 °C). The anti-MUC1

aptamer hairpin structure consists of two double-stranded stems, a loop and a bulge (Figure 1-20). The primary stem is comprised of four base pairs (residues 8 – 11 and 15 – 18) connected to a loop made up of three thymines (residues 12 – 14) and a mismatched bulge which is connected to a short three base-pair stem (residues 2 – 4 and 22 – 24). The melting point of this secondary structure was calculated to be 36.1 °C[104].The radioisotope-labelled anti-MUC1 aptamer was either folded into its hairpin configuration by slow cooling following high temperature melting or deliberately randomly folded by rapidly cooling via submersion into liquid nitrogen following high temperature melting. A trace amount (< 2 nM) was then allowed to bind to various concentrations of the 40-mer 2×VTR or the 60-mer 3×VTR MUC1 peptide overnight prior to polyacrylamide gel electrophoretic mobility shift assays.

In the electrophoretic mobility shift assays of the 3×VTR MUC1 peptide, a band shift can be observed at 70 μM (Figure 2-3a) in the assay with the folded aptamer; the shift is not observed in the "unfolded" aptamer assay (Figure 2-3b). However, in the electrophoretic mobility shift assay of the 2×VTR MUC1 peptide, no binding can be seen up to 70 μM peptide concentration in both the assay with folded and "unfolded" aptamers (Figure 2-4). Using ImageJ software to analyze the gels, it was found that the intensity ratio of the bound to unbound band in the 70 μM 3×VTR peptide gel lane is 90:10; an estimate of the dissociation constant can be made accordingly. The K_d of the 25-nt aptamer to the 3×VTR MUC1 peptide under these binding conditions is between 60 – 70 μM. Due to insufficient peptides, further gel shift assays was determined to be an unwise use of resources, especially in light of the fact that the dissociation constant of the anti-MUC1 aptamer in solution is not necessary for the primary objective of this work, which is to characterize the immobilized hairpin anti-MUC1 aptamer on a electrochemical sensor.

Figure 2-3: Electrophoretic mobility shift assay of 3×VTR MUC1 peptides

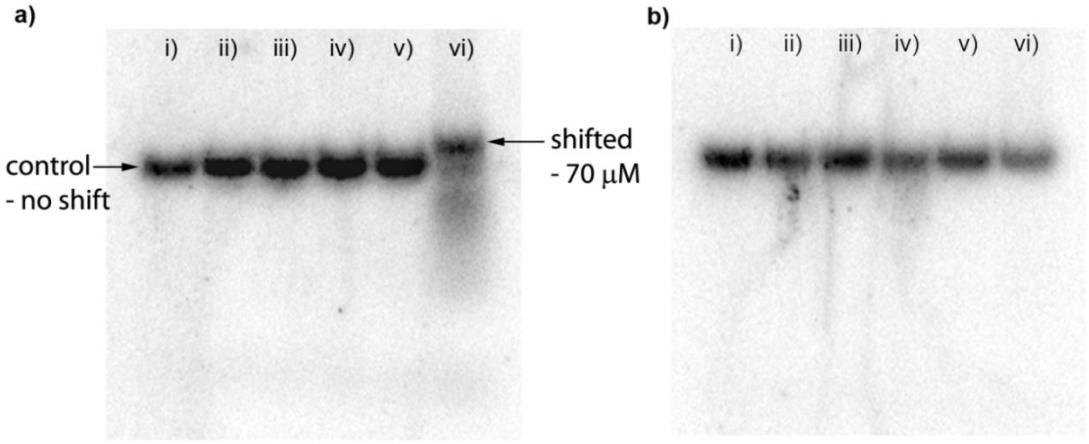

Gel shifts of a) folded and b) unfolded 25-mer anti-MUC1 aptamer (<4 nM) and the 3×VTR MUC1 peptide. For each graph: i) control - no peptide, ii) 30 µM, iii) 40 µM, iv) 50 µM, v) 60 µM, vi) 70 µM 3×VTR MUC1 peptide. The 10% native polyacrylamide gel was cast and ran in buffer consisting of 100 mM Tris, 50 mM NaCl and 5 mM MgCl2 (pH ~8).

Figure 2-4: Electrophoretic mobility shift assay of 2×VTR MUC1 peptides

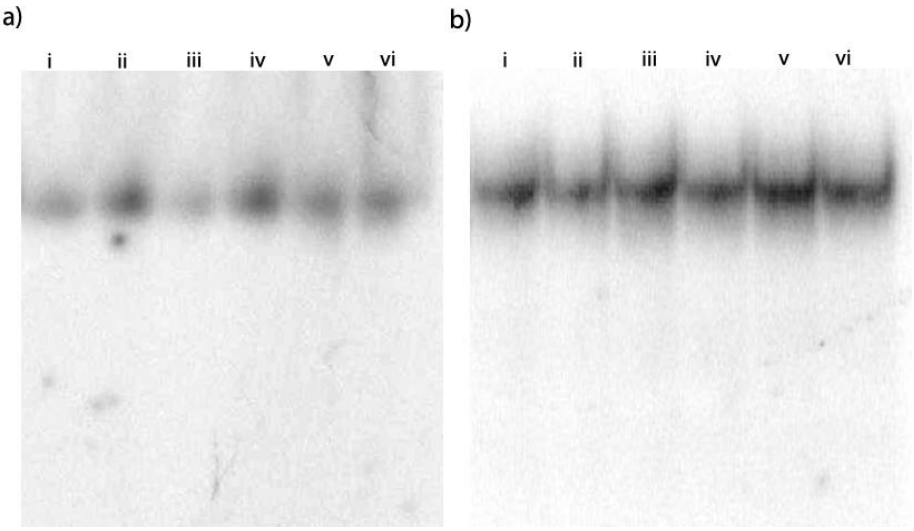

Gel shift assay of a) folded and b) unfolded 25-mer anti-MUC1 aptamer (<4 nM) and the 2×VTR MUC1 peptide. For each graph: i) control - no peptide, ii) 30 µM, iii) 40 µM, iv) 50 µM, v) 60 µM, vi) 70 µM 2×VTR MUC1 peptide. The gels were run under the same conditions as Figure 2-3.

Ferreira et al. selected the 25-nt anti-MUC1 aptamer using the synthetic 60-mer 3×VTR peptide[103] and attached the biotinylated peptide onto a gold surface and found the dissociation constant to be 0.135 nM via surface plasmon resonance spectroscopy. One possible reason for the discrepancy is the limitation of electrophoretic gel shift assays, i.e. during the process of electrophoresis the peptide-aptamer complex may not be in an equilibrium state[113]. It is assumed that once the complex enters the gel, the effect of dissociation and re-association of the complex cancel each other out as the polyacrylamide matrix will prevent the dissociated peptide and aptamer from diffusing away from each other[113]. However, during loading, there is a possibility that the complex may break apart due to the attractive force that pulls the highly negatively charged aptamer towards the anode being much stronger than the attractive force that pulls on the peptide[112]. High initial voltages, reduced salt concentrations (50 μM), lower temperatures (4 °C) and shorter run times were used in an attempt to minimize this probability. Regardless, the difference in attractive force also affects the aptamer-peptide complex once it enters the polyacrylamide matrix[112], therefore it is possible that the peptide-aptamer complex was not stable over the course of the electrophoresis timeframe. Nevertheless, we were able to confirm the binding between this anti-MUC1 aptamer with the target analyte (MUC1).

2.3. Conclusions

Using standard gel electrophoresis shift assay, the dissociation constant of the 25 nt anti-MUC1 aptamer for the 3×VTR MUC1 peptide was estimated to be 60 to 70 μM. It was discovered that the binding only occurs if the aptamer was folded into the hair-pin structure, indicating that the folded hairpin aptamer is most likely required for binding. As a control experiment, the dissociation constant of anti-CTAP III/NAP 2 aptamer for the NAP 2 protein was also determined; the obtained value (0.118 μM) is consistent with that determined previously in our laboratory. Most importantly, this

control experiment confirms that the challenges of the gel shift of anti-MUC1 are not related to any issues in experimental techniques.

3. Electrochemistry of the anti-MUC1 aptamer-modified electrodes

The analytical advantages of the electrochemical sensors make them an ideal platform in the design of portable, point-of-care biosensors. Their excellent sensitivity, with a very large linear detection range, combined with the versatility of aptamers opens up endless possibilities for creating fast, accurate electrochemical sensors. Ever since aptamers were first discovered over two decades ago[10,11], the use of aptamers in sensors, and especially electrochemical sensors, have been a very active area of research[12,20-22,35,114-116]. Nevertheless, there has been limited success for commercial aptamer-based electrochemical biosensors; this is likely due to the variation in sensor response to the target between individual electrodes. This work is an investigation into the effect of aptamer surface density on electrochemical sensor response using the hairpin anti-MUC1 aptamer and the synthetic MUC1 peptides.

3.1. Experimental

3.1.1. Reagents

HPLC-purified and desalted dual methylene blue (MB) / thiol end-modified oligonucleotide (HO-$(CH_2)_6$-SS-$(CH_2)_6$-O-5'-GCA GTT GAT CCT TTG GAT ACC CTG G-3'-$(CH_2)_7$-NHCO-$(CH_2)_3$-MB) was purchased from Biosearch Technologies, Inc. (Novato, CA); the mass was confirmed using LC-MS performed by Biosearch Technologies, Inc. (Figure 3-1). The 40-mer 2×VTR MUC1 and 60-mer 3×VTR peptides were obtained and

purified as described previously (Section 2.2.1). All other reagents were of reagent grade and used without further purification.

Figure 3-1: LC-MS spectra of dual-labeled anti-MUC1 aptamer

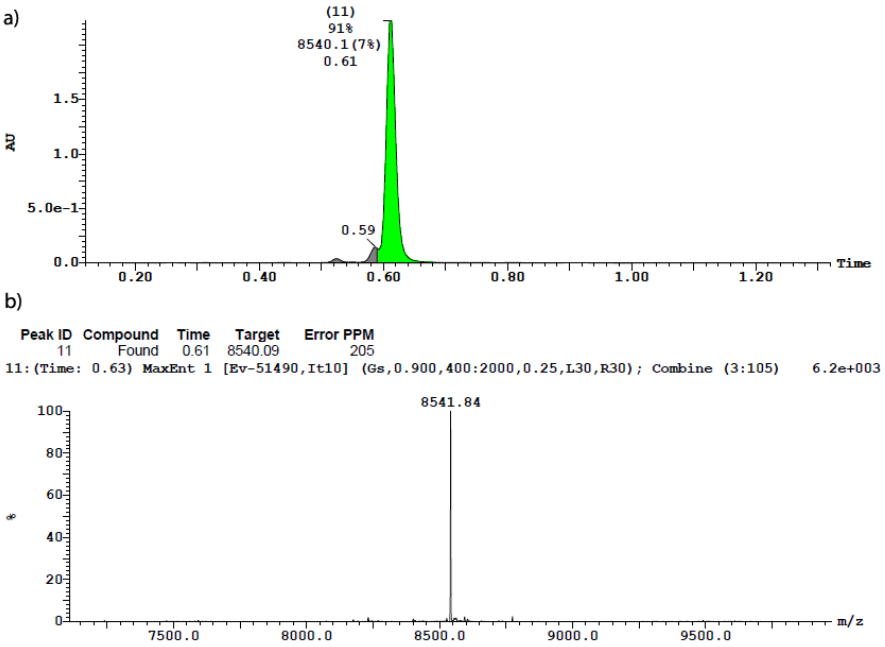

Figure 3-1a) shows the HPLC chromatogram and Figure 3-1b) shows the mass spectra. Figures provided by Biosearch Technologies, Inc. (Novato, CA).

3.1.2. Electrode preparation

All of the following procedures were performed in the dark, except the gold cleaning procedure, because the redox marker methylene blue absorbs visible light and generates singlet oxygen in air which will damage the DNA strands. Dual thiol and MB-modified anti-MUC1 aptamers were treated with 10 mM tris(2-carboxyethyl)phosphine (TCEP) in 100 mM Tris buffer (pH 7.4) for 20 hours. The buffer was then exchanged with deaerated 100 mM Tris, 100 mM NaCl, 5 mM $MgCl_2$, pH 7.4 buffer (binding buffer 2) using Illustra MicroSpin G-25 columns (*GE Healthcare*). The samples were then heated to 80 °C for 5 min and allowed to cool slowly to room temperature in order to fold into the

proper secondary structures. Deaerated binding buffer 2 was added prior to surface immobilization to generate solutions of 1 to 30 μM aptamer concentrations.

A 1.5×2.5-cm^2 piece of gold-coated glass slide (100 nm Au on 10 nm Cr, purchased from Evaporated Metals Films, Inc., Ithaca, NY) was cleaned by immersion into a heated solution of piranha (1:3 30% H_2O_2: concentrated H_2SO_4) for 8 minutes. (Warning! This solution is highly reactive; proper precautions must be taken during use.) The slide was then rinsed thoroughly with deionized water (*Thermo Scientific Barnstead, Inc. Easypure UV/UF Water Purification Station model D8611*); excess water was blown off the gold surface with nitrogen.

20 μL of an aptamer solution was then placed onto the gold slide and allowed to immobilize onto the surface in a darkened chamber for 16 hrs. with 100% relative humidity. The aptamer-modified gold electrode was then washed with binding buffer 2 and excess buffer was blown off the gold surface with nitrogen. 20 μL of 1 mM 6-mercaptohexan-1-ol (MCH) in binding buffer 2 was then placed onto the electrode for an hour in the dark chamber in order to passivate the gold surface. The electrode was then washed with binding buffer 2 and excess buffer was blown off the gold surface with nitrogen. The electrode was assembled into a PTFE electrochemical cell that allows for an exposed electrode surface area of 0.225 cm^2 that is sealed with a rubber O-ring.

3.1.3. Electrochemical measurements

Cyclic voltammetry (CV) was performed on a CHI1040A potentiostat (*CH Instruments, Inc.*) in deaerated binding buffer 2 at various scan rates from approximately 0 V to -0.8 V (depending on the scan rate). Alternating current voltammetry (ACV) was performed on the same potentiostat from -0.15 V to -0.5 V at 100 Hz with an amplitude of 25 mV. A Ag|AgCl reference electrode in saturated KCl and a Pt wire counter electrode were used during the measurements.

After the initial scans, various concentrations of 2×VTR MUC1 or 3×VTR in binding buffer 2 were placed onto the electrode. The 2×VTR peptides were allowed to bind overnight in the darkened chamber with 100% humidity. The electrodes exposed to 2×VTR peptides were then briefly washed with deaerated binding buffer 2 prior to being examined using CV and ACV in binding buffer 2 in the same manner as above. The electrodes exposed to the 3×VTR peptides were allowed to bind for an hour in the darkened chamber with 100% humidity. These electrodes were examined without washing and in the presence of the peptide using CV at various scan rates and ACV.

3.2. Results and discussion

3.2.1. Electrochemical characterization of anti-MUC1 aptamer modified gold electrodes

Structural changes of the immobilized aptamer probes due to target binding are a common motif in the design of aptamer-based electrochemical sensors[117,118]. In this work, the methylene blue (MB)-labelled anti-MUC1 aptamer is first "folded" into the hairpin secondary structure and then immobilized onto the gold electrode surface via thiol-gold linkages. As shown in Figure 3-2, we expect that the redox active MB at the 3'-end would be close to the 5'-end and proximal to the electrode surface, which will allow for facile electron transfer between MB and gold electrode. We hypothesize that upon binding to the target peptide, the electrochemical signal from the MB will be significantly reduced due to the peptide binding and unfolding the aptamer thus increasing the distance between MB and the electrode[119].

Figure 3-2: The two dimensional structure of the folded hairpin anti-MUC1 aptamer on the surface of the gold electrode.

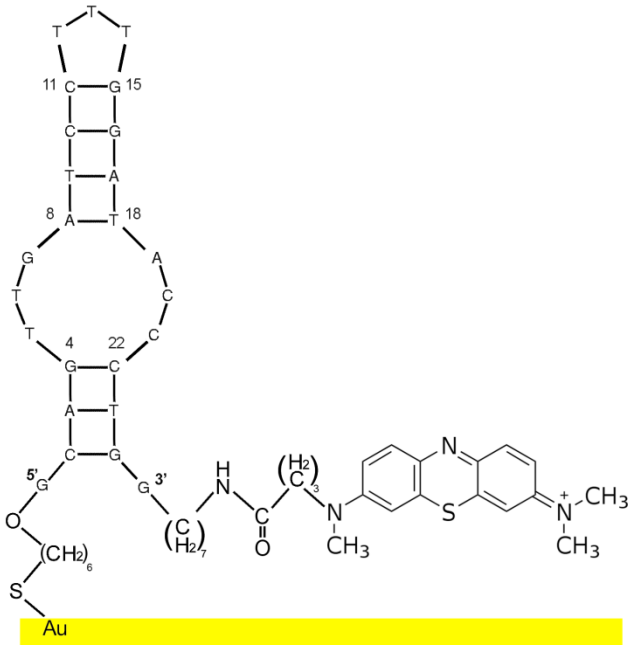

Cyclic voltammetry was performed on anti-MUC1 aptamer-modified gold electrodes of different surface densities at various scan rates in order to characterize their redox properties. The cyclic voltammograms of the electrodes shows reversible redox behaviour; the symmetric reduction and oxidation peaks (Figure 3-3a) correspond to the two-electron, one protonation reduction from methylene blue (MB) to leucomethylene blue (LB) (Figure 3-4).[120] The two electron transfer steps are fast and cannot be distinguished by cyclic voltammetry[120]. The plot of the cathodic peak current vs. scan rate, Figure 3-3b, which reveals a linear relationship between the two, confirms the fact that MB redox centres are immobilized on the electrode surface.

Figure 3-3: Cyclic voltammogram of anti-MUC1 modified electrodes

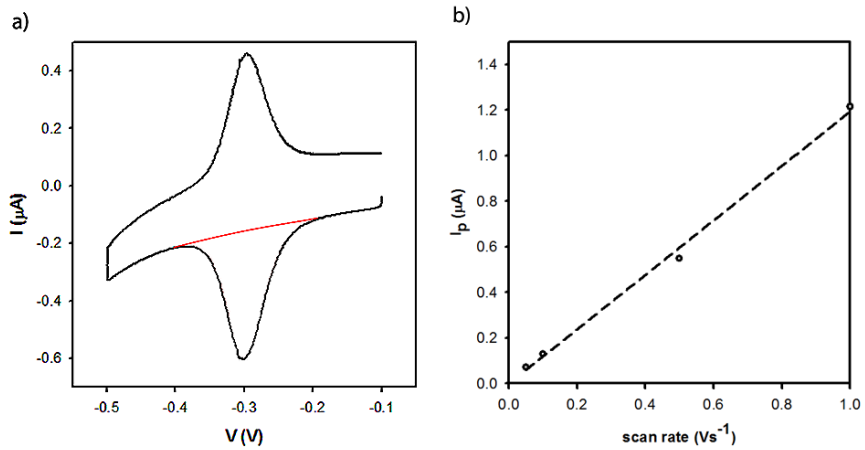

a) Cyclic voltammogram of an aptamer-modified gold electrodes surface with a surface density of 1.09×10^{12} molecules/cm^2 (scan rate = 100 mV/s). The red line shows the baseline current used for integration for charge (Q). b) The cathodic peak current vs. scan rate plot reveals a linear relationship at low scan rates (< 1 V/s) signifying surface dependent electrochemistry. Potentials were measured against a Ag|AgCl reference electrode in saturated KCl.

Figure 3-4: Redox mechanism for methylene blue

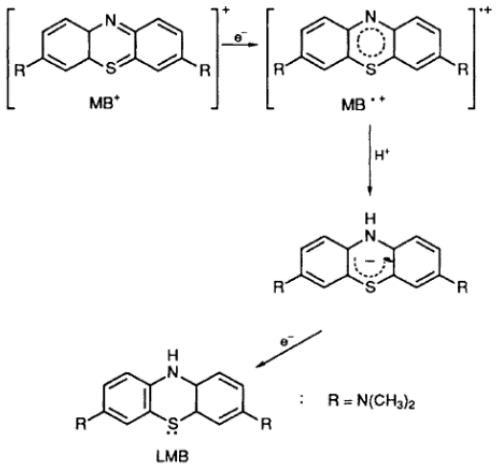

Redox reaction of methylene blue (MB) to leucomethylene blue (LB) at the electrode surface is a very fast two electrons, one proton process[120]. Figure adapted from reference [120].

The surface density (concentration) of aptamers on the electrode surface can be calculated using the following equation:

$$\Gamma_{MB} = \frac{QN_A}{nFA} \qquad \text{(Eq2)}$$

where Γ_{MB} is the surface coverage (surface concentration in molecules/cm^2) of aptamer strands immobilized on gold electrode, *Q* is the charge integrated from the current of the cathodic peak (as shown in Figure 3-3a), *n* is the number of electrons involved in the redox reaction, *F* is Faraday's constant, N_A is Avogadro's number and *A* is the electrode area. Assuming that every MB on the surface is electroactive, we can then determine the surface density of aptamers on the electrode. Despite the fact that we tried to fold the aptamers into its hairpin secondary structure via high temperature melting followed by slow cooling to room temperature (~22 °C) prior to immobilization onto the gold surface, we have observed significant variations in the surface density between samples; even in electrodes prepared simultaneously the surface density will slightly differ, albeit less substantially. The histogram of the distribution of surface densities from more than 20 trials shows two distinct surface density distributions (Figure 3-5). The low density distribution is centered around 5×10^{11} molecules/cm^2 the high density distribution is centered around 4×10^{12} molecules/cm^2. The midpoint between the two is around 2×10^{12} molecules/cm^2 and as a result, this is where we drew the dividing line between high and low density surfaces for the purpose of discussion. The bimodal surface density distribution has not been observed for aptamers that do not have a hairpin structure, for example, anti-lysozyme aptamers (Figure 3-6). Although all the electrodes were prepared in the same manner, it is also possible for the hairpin aptamers to interact with each other during the folding process to form intermolecular structures held together by short duplex regions. These aptamer strands will immobilize closely onto the electrode, creating a denser DNA monolayer on the electrode surface. It is also possible that the aptamers unfold during the hours-long immobilization process, thus forming surfaces with higher densities.

Figure 3-5: Histogram of anti-MUC1 aptamer surface coverage

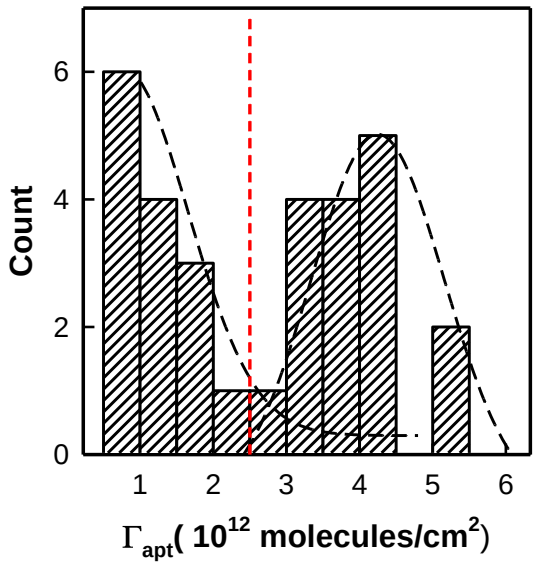

Histogram shows two distinct distributions attributed to different secondary structures of the surface immobilized aptamer. Sensors with low surface density are likely to consist of well-folded aptamers whereas sensors with high surface density are likely to consist of "unfolded" aptamers more tightly packed together.

Upon adding the analyte (either 2×VTR or 3×VTR MUC 1 peptide) to the system, we have observed clear changes in the voltammetric response, i.e., both cathodic and anodic peaks decreases. To better illustrate the response, we carried out ACV measurements on the anti-MUC1 modified gold electrodes (Figure 3-7). Although sensors with higher surface densities (≥ 2 × 10^{12} molecules/cm^2) started initially with high peak current and area, they showed almost no change in their ACV peak current upon exposure to the MUC1 peptides (Figure 3-7b). Under identical experimental conditions, electrodes with lower surface densities (had lower peak current to start with) demonstrated a definite decrease after introduction of MUC1 (Figure 3-7a). In particular, upon adding 10 μM 2×VTR MUC1 to the electrolyte, a 35% decrease in the ACV peak current was observed; in contrast, the change in the peak current is much less for high-density surfaces (~ 2% for 2×VTR peptides, ~8% for 3×VTR peptides).

Figure 3-6: Histogram of anti-lysozyme aptamer surface coverage

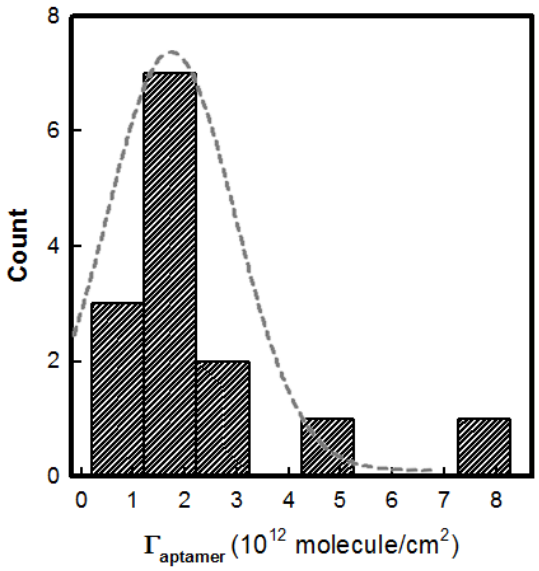

Histogram of the anti-lysozyme aptamer shows only a single distinct surface density distribution of aptamers on aptamer-modified electrodes. Unlike "hairpin" aptamers that can have a well-folded structure, the anti-lysozyme aptamer does not have such a "hairpin" secondary structure and does not show two surface density distributions.

Figure 3-7: Alternating current voltammetry with 2×VTR peptides

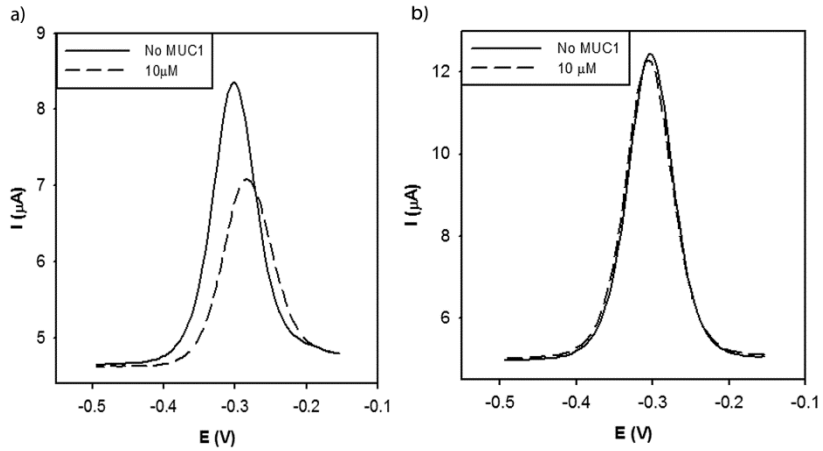

ACV of low (a) (1.04×10^{12} molecules/cm^2) and high (b) (2.99×10^{12} molecules/cm^2) density electrode surfaces with 10μM 2×VTR MUC1aptamer.

We hypothesize that the two surface-density distributions and their respective sensing responses may be due to the two possible three-dimensional configurations that the immobilized aptamer can take on the surface (Figure 3-8). A well-folded and orderly packed aptamer monolayer surface will have a lower surface density due to steric hindrance. If we assume an even distribution across the surface, the intermolecular distance between the aptamers is approximately 5 nm in an electrode with a surface density of 2×10^{12} molecules/cm^2. This monolayer is not very dense thus the spacing between aptamer strands may allow the larger peptide come in close to the electrode surface to bind. Unfolded aptamers, on the other hand, will immobilize onto the surface in a random manner giving a more tightly packed monolayer of single-stranded DNA that may not permit peptide binding. Also, in a higher density monolayer a portion of the MB redox marker may already be held far above the surface initially and will not show a change in the electrochemical response upon MUC1 binding. This same sensor response phenomenon has also been seen in electrochemical DNA hybridization sensors[46,48,121] and is attributed as one of the causes of sensitivity differences between different research groups[46]. Cheng et al. recently reported an electrochemical lysozyme sensor that used an electrostatic redox marker, ruthenium (III) hexamine, to monitor target binding[49]. The sensor signal showed the optimum response in sensors with aptamer surface densities between $1.6 – 1.8 \times 10^{12}$ molecules/cm^2 with decreases in sensor sensitivity when the surface density increases. Another possible reason for limited sensor response is that the folded hairpin aptamer secondary structure, which is favoured thermodynamically, may be a prerequisite for binding to MUC1 and is found in smaller amounts in a highly dense surface.

Figure 3-8: Schematic depicting the two possible conformations of anti-MUC1 aptamers on the electrode surface.

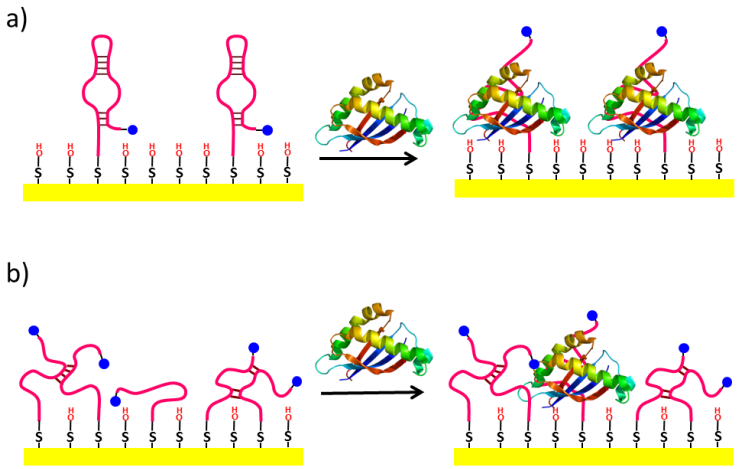

(a) Well-folded aptamers pack less densely on the gold electrode surface but allows for peptide binding while (b) unfolded aptamers can pack more densely and can interact with each other and thus limit peptide binding.

We have noted that our sensor response is dependent on the time required to equilibrate the system after the analyte is introduced. As shown in Figure 3-9a), with 2 mL quick rinses of the electrode surface after binding and detection in the absence of the peptide, the 2×VTR peptide requires 6 hrs. for the sensor to reach equilibrium, as a result, overnight binding was chosen in the initial stages of this work. However, as it became apparent that the gel shift assays was not able to detect any binding for the 2×VTR peptide, our attention shifted towards the 3×VTR peptide. Due to the high dissociation constant of the 3×VTR peptide for the anti-MUC1 aptamer, found in the gel shift assays, it was decided that the sensor should not be washed prior to detection but rather kept in the presence of the peptide. It takes the electrodes approximately 5 min for the electrochemical signal to reach the equilibrium levels using this protocol (Figure 3-9b). Ferreira et al. used an equilibration time of one minute in their SPR experiments to determine the dissociation constant[103] but found that it required multiple 30-second washes to remove the aptamer from the peptide-modified gold surface. This shows that the binding kinetics of the aptamer to the peptide is most likely to be in the order of

minutes while the dissociation kinetics is slower. As the sensor response time dictates the downstream application, faster binding kinetics and short response time is desirable for real-time sensor applications.

Figure 3-9: Time dependence plots

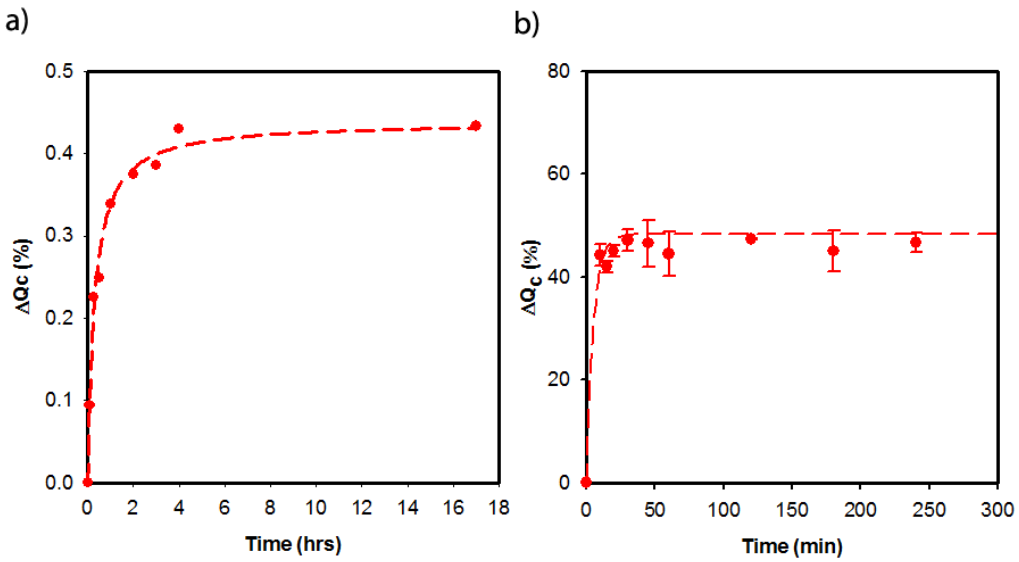

Time dependence plot showing time to reach binding equilibrium a) 2×VTR peptide binding (with washing) showing equilibrium after 6 hours and b) 3×VTR peptide binding (without washing) showing that 30 minutes is required for the system to reach equilibrium. ΔQ_c is the percent decrease in the signal of the cyclic voltammograms.

In the concentration dependence plot, the electrochemical response increases as the concentration of 2×VTR peptide becomes higher for the low surface density sensors until it reaches saturation near 2 μM MUC1, even though less than 30% decrease of the original electrochemical signal was observed (Figure 3-10). The dynamic range of this sensor for 2×VTR is between 1 to 10 μM and the limit of detection is approximately 1 μM. There is not enough data to create a concentration dependence curve for the binding of 3×VTR peptide. For the high surface density electrodes, no 2×VTR concentration dependent (Figure 3-10) or 3×VTR concentration dependent (Figure 3-11) response can be observed. The detection limit and linear region of this low surface

density MUC1 sensor may not be impressive compared to the QD-based fluorescence sensor with a lower detection limit (250 nM) and a linear response range up to 2 μM[102], however, the "cut-off concentration" of MUC1 in a normal healthy women is generally accepted to be 35 U/mL which corresponds to approximately 5 μM MUC1[102]; the electrochemical version of the MUC1 sensor should be able to accommodate such a test.

Figure 3-10: 2×VTR peptide concentration vs. electrochemical response

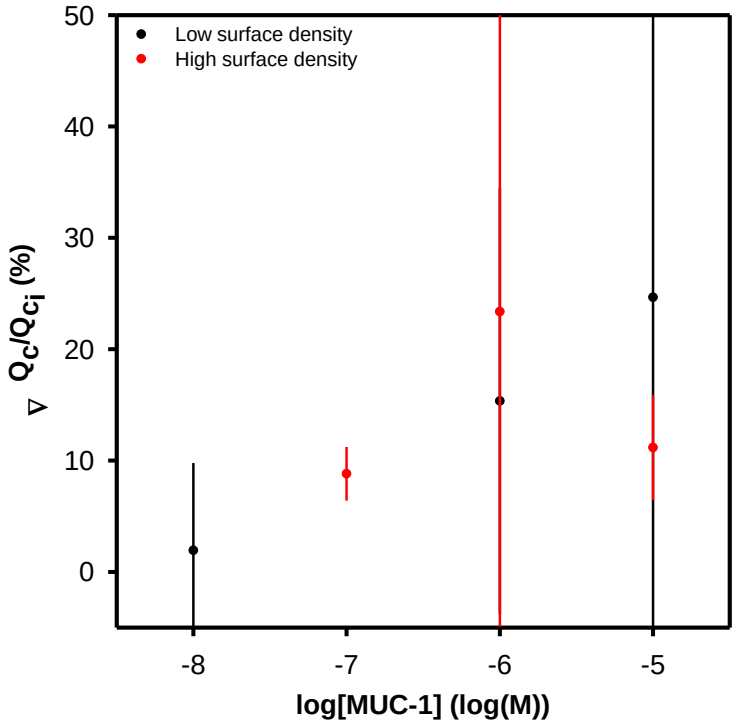

Concentration vs. change in the cathodic charge of aptamer-modified electrodes with high aptamer surface density (open circles) and low aptamer surface density (closed circles) after introduction of the 2×VTR peptide. This plot combines data from 30 unique sensors; the relative error for each data point is significant due to the differences in surface density of each individual sensor but was left out for visual clarity.

Figure 3-11: 3×VTR peptide concentration vs. electrochemical response

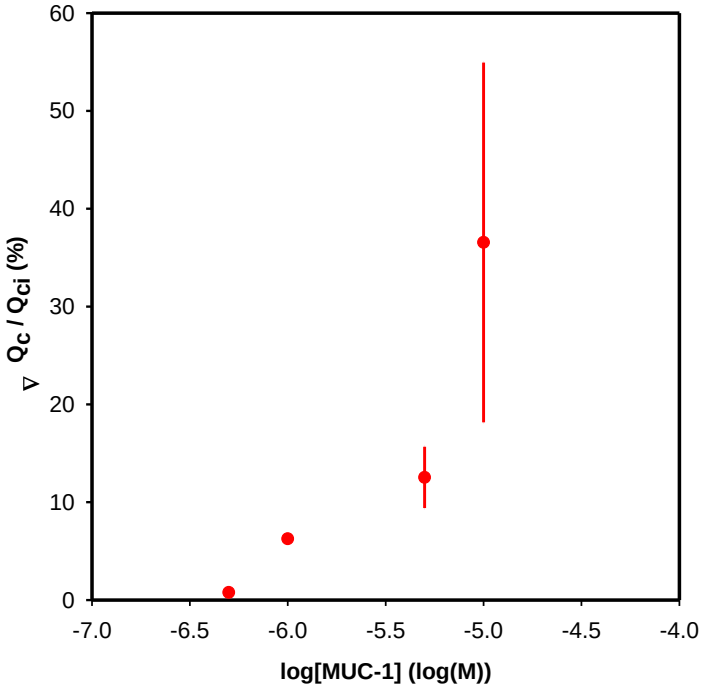

Concentration vs. change in the cathodic charge of aptamer-modified electrodes with high aptamer surface density after binding to the 3×VTR peptide. Errors bars are due to the compilation of multiple electrodes with different surface densities (> 2×10^{12} molecules / cm^2).

In order to overcome the limitations in the sensitivity and dynamic response range, the preparation of the ideal sensor electrode with optimal surface density is required, but this proved to be challenging. Although the aptamers were carefully treated by melting in high temperatures and very slowly cooled to low temperatures, it was difficult to reproducibly create well-ordered hairpin aptamer electrodes. Attempts to control the surface density by controlling the concentration of aptamers have been used successfully in the past by other groups[41], but had limited success in this work; alternatively, attempts to control the deposition of DNA onto electrodes using applied potentials have also been reported[122-124]. A possible explanation of this variability may be that the self-complementary regions of the aptamer can also hybridize

intermolecularly with other aptamers, forming aptamer dimers which will affect the subsequent surface immobilization.

3.2.2. Surface density effects on electron transfer kinetics

An important feature of the present system is the ability to study the electron transfer process between the redox centres tethered at the end of the hairpin DNA aptamer and the electrode. Figure 3-12a show the effect of scan rate on the peak potentials in cyclic voltammograms. According to the classical model developed by Laviron[125], in a diffusionless system (i.e. surface-immobilized redox markers), when the overpotential is large, the electrochemical system can be treated as if the redox reaction was irreversible (i.e. only reduction or oxidation reaction will occur on the electrode). At higher scan rates when the cathodic and anodic peak separation is greater than 200/*n* mV (*n* is the number of electrons in the reaction), it is possible to obtain the apparent electron transfer rate constants from the following equations[126]:

$$E_{pc} = E° - \left(\frac{RT}{\alpha nF}\right)\ln\left(\frac{\alpha nF\nu}{RTk}\right) \quad \text{(Eq3)}$$

$$E_{pa} = E° - \frac{RT}{(1-\alpha)nF}\ln\left(\frac{(1-\alpha)nF\nu}{RTk}\right) \quad \text{(Eq4)}$$

where E_{pc} and E_{pa} are the cathodic and anodic peak potentials, $E°$ is the standard redox potential, ν is the scan rate, α is the electron transfer coefficient, k is the rate constant and R, T, n and F have the standard definitions. The plot of $E_p - E°$ vs. ln ν will give two straight lines at high scan rates whose slope are $-RT/\alpha nF$ and $RT/(1-\alpha)nF$ for the cathodic and anodic portion, respectively (Figure 3-12b).

Figure 3-12: Scan rate dependence of electrochemical response in cyclic voltammetry

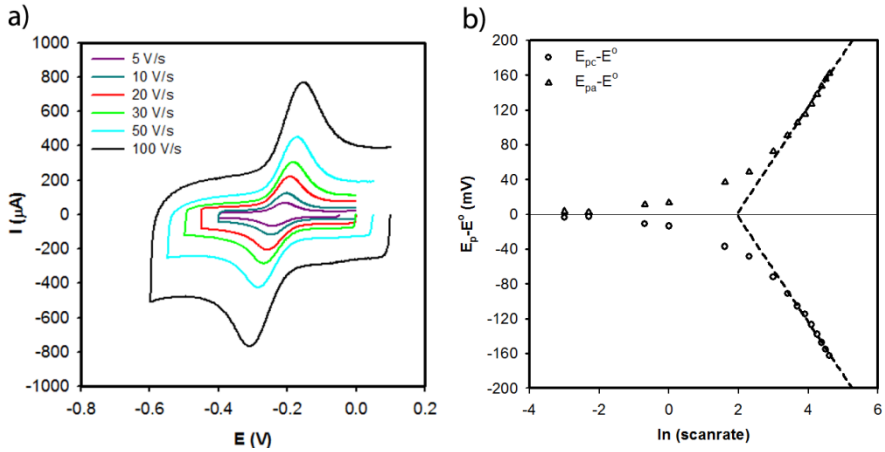

a) As the scan rate increases, peak separation increases as a result of mass transport limitations at the electrode surface. b) A representative Laviron plot showing the linear region (dotted line) at high scan rates where irreversible redox behavior can be approximated.

The rate of electron transfer was found to vary significantly at different aptamer surface densities; higher surface densities resulted in much slower electron transfer kinetics. In a plot of *k* vs. surface density ($\Gamma_{aptamer}$) (Figure 3-13), it is clear that *k* remains relatively unchanged at approximately 425 s^{-1} when the surface density is less than 2×10^{12} molecules/cm^2, while at surface densities greater than 2×10^{12} molecules/cm^2, the value of *k* decreases sharply. We propose that this may be a result of the "folded" hairpin secondary structure of the immobilized anti-MUC1 aptamers in the low surface density electrodes holding the MB redox centre close to the electrode surface (Figure 3-8a), giving a faster apparent electron transfer rate. Evidently, the electron transfer kinetics are not dictated by the surface density when it is below 2×10^{12} molecules/cm^2. For the "unfolded" aptamers in the higher surface density electrodes (Figure 3-8b) the apparent electron transfer rates are "controlled" by the surface density; higher surfaces densities end up with sluggish electron transfer kinetics.

Figure 3-13: Dependence of electron transfer kinetics on surface density

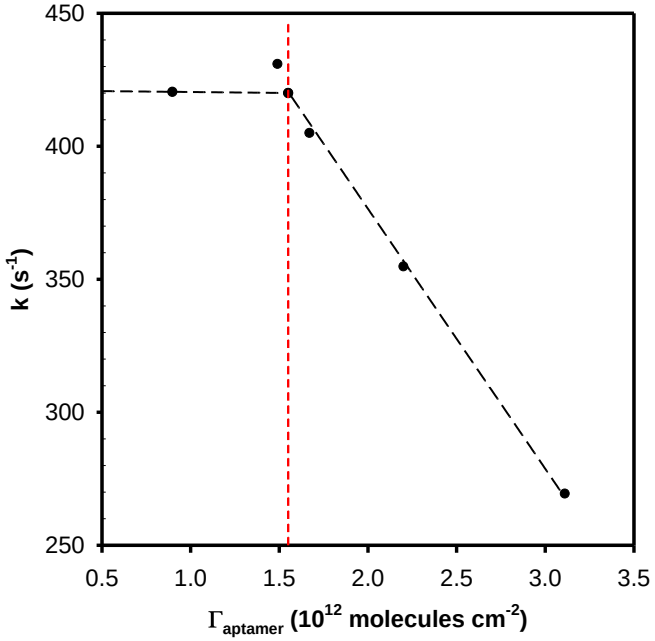

Following Laviron's model described above[124], the values of k were calculated and plotted against aptamer surface density. At higher density the reaction rate drops, while at lower surface density the reaction rate is stable. The dashed lines are drawn to help guide the eye.

It has been reported that in surface-bound, end-labelled, flexible, single-stranded oligonucleotides, the apparent electron transfer rate is inversely proportional to DNA length due to the rate limiting approach of the labelled ends to the electrode which can be described by the following equation[62]:

$$k_{app} \propto \left(N l_p\right)^{-1} \qquad \text{(Eq5)}$$

where k_{app} is the apparent electron transfer rate constant, N is the number of nucleotides and l_p is the persistence length of the oligo, (the shortest "flexible" length of ssDNA strand, approximately the length of 3 – 4 nucleotides). The apparent electron transfer rate for a 25 nt ssDNA was reported to be approximately 100 s^{-1} for electrodes with

surface densities of ~9.3×10^{12} molecules/cm^2 [62]. It is interesting to note that the electron transfer rate of our high surface density electrode is of the same order as those reported previously[62]. In our low density sensors, the folded aptamers hold the MB redox label closer to the surface and in a "stiffer" fashion, thus increasing the rate of electron transfer. Anne and Demaille proposed that in rigid double helices attached onto an electrode via longer alkanethiol linkers ($\geq C_6$), the primary electron transfer mechanism is the result of the free-motion of the alkanethiol linkers flexing that allow the end-labelled redox markers to collide with the electrode[127] (Figure 3-14).

Figure 3-14: Schematic of electron transfer at redox labelled ds-DNA electrodes

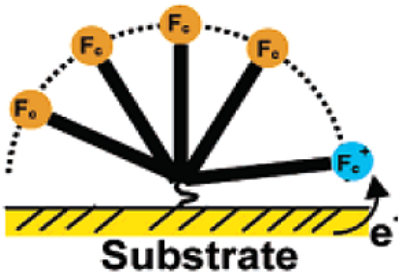

Schematic depicting the electron transfer process of a ferrocene redox marker at the end of a rigid double-stranded oligo immobilized onto an electrode substrate. Reprinted with permission from [61]. Copyright (2007) American Chemical Society.

3.3. Conclusions

The performance of aptamer-based electrochemical sensors is dependent on the surface properties of the aptamer monolayer on the electrode. Particularly for the hairpin DNA aptamer for MUC1, high surface densities do not provide better responses; lower surface densities create a better performing sensor as a result of lower steric hindrance and proper folding towards the target binding. The electron transfer kinetics of the different electrodes are dictated by the surface density of the hairpin DNA aptamer; the two different folding states yields different trends in the electron transfer

kinetics. Most importantly, this work confirms that a better design of aptamer-based electrochemical sensors can be achieved by carefully controlling the surface density and folding structure of DNA aptamers on electrode surface.

4. Conclusions

4.1. Summary

In this work we have shown that the surface densities of aptamer-modified electrodes have a significant effect on the electrochemical response of the sensor. The ability to control surface densities will allow for the production of sensors with reproducible responses; however, we have found that it is not easy to control surface densities, especially for aptamers with complex secondary structures or aptamers with self-complementary regions. For the hairpin DNA anti-MUC1 aptamer, in particular, we have found the surface densities of the aptamer-modified electrodes to be divided into two distinct distributions, despite attempts to regulate the deposition process by controlling the aptamer concentration of the deposition buffer. Electrodes with surface densities $> 2.0 \times 10^{12}$ molecules / cm^2 have limited sensor response to both the 2×VTR and 3×VTR peptide target, while electrodes with surface densities $<2.0 \times 10^{12}$ molecules / cm^2 have far greater response to the target. Different densities dictate the electron transfer kinetics which show a distinct change in behavior at densities greater than 2.0×10^{12} molecules / cm^2.

4.2. Future Works

Further work into the effect of surface density on aptamer-based electrochemical sensors will be beneficial for future sensor designs. Experiments on the aptamer immobilization conditions (such as salt concentrations, aptamer concentrations and temperature) are necessary to refine the sensor manufacturing protocol. Improvements

in aptamer immobilization methods that will allow for better control of the deposition process and lead to better reproducibility which will assist in bringing these very promising biosensors towards commercialization.

4.3. Conclusion

Although higher surface density sensors have higher initial electrochemical response, which is preferable for “signal-off” sensors like this MUC1 sensor, higher surface density will also lead to slow electrode kinetics and limited target response. On the other hand, low surface densities have lower initial electrochemical response and are less desirable. “Signal-on” sensors do not have this issue. Future designs of aptamer-based electrochemical sensors should take this effect into account. This work confirms that a better design of aptamer-based electrochemical sensors can be achieved by carefully controlling the surface density and folding structure of DNA aptamers on electrode surfaces.

5. References

(1) Wang, J. *Chem. Rev.* **2008**, *108*, 814

(2) *Life First: OneTouch*; Life First: http://www.onetouch.com/ultramini, 2010.

(3) Xiang, Y.; Zhang, Y. Y.; Qian, X. Q.; Chai, Y. Q.; Wang, J.; Yuan, R. *Biosens. Bioelectron.* **2010**, *25*, 2539.

(4) Lodish, H.; Berk, A.; Zipursky, S. L.; Matsudaira, P.; Baltimore, D.; Darnell., J. *Molecular Cell Biology*; 4th Edition ed.; W. H. Freeman and Company: New York, 2000.

(5) Metzler, D. E. *Biochemistry: The Chemical Reactions of Living Cells*; Academic Press, Inc.: New York, 1977.

(6) Watson, J. D.; Crick, F. H. C. *Nature* **1953**, *171*, 964.

(7) Crick, F. H. C. *Proc. Nat. Aca. Sci.* **1954**, *40*, 756.

(8) Sínanoğlu, O.; Abdulnur, S. *Photochem. Photobiol.* **1964**, *3*, 333.

(9) Dickerson, R. E.; Drew, H. R.; Conner, B. N.; Wing, R. M.; Fratini, A. V.; Kopka, M. L. *Science* **1982**, *216*, 475.

(10) Ellington, A. D.; Szostak, J. W. *Nature* **1990**, *346*, 818.

(11) Tuerk, C.; Gold, L. *Science* **1990**, *249*, 505.

(12) Tombelli, S.; Minunni, M.; Mascini, M. *Biomol. Eng.* **2007**, *24*, 191.

(13) Homann, M.; Goringer, H. U. *Nucleic Acids Res.* **1999**, *27*, 2006.

(14) Huang, Y.-F.; Shangguan, D.; Liu, H.; Phillips, J. A.; Zhang, X.; Chen, Y.; Tan, W. *ChemBioChem* **2009**, *10*, 862.

(15) Bruno, J. G. *In Vitro Cell. Dev. Biol.-Anim.* **2010**, *46*, 107.

(16) O'Sullivan, C. *Anal. Bioanal. Chem.* **2002**, *372*, 44.

(17) Hermann, T.; Patel, D. J. *Science* **2000**, *287*, 820.

(18) Tang, Z.; Shangguan, D.; Wang, K.; Shi, H.; Sefah, K.; Mallikratchy, P.; Chen, H. W.; Li, Y.; Tan, W. *Anal. Chem.* **2007**, *79*, 4900.

(19) Wang, C.; Zhang, M.; Yang, G.; Zhang, D.; Ding, H.; Wang, H.; Fan, M.; Shen, B.; Shao, N. *J. Biotechnol.* **2003**, *102*, 15.

(20) Cerchia, L.; Hamm, J.; Libri, D.; Tavitian, B.; de Franciscis, V. *FEBS Letters* **2002**, *528*, 12.

(21) Brody, E. N.; Willis, M. C.; Smith, J. D.; Jayasena, S.; Zichi, D.; Gold, L. *Mol. Diag.* **1999**, *4*, 381.

(22) Dausse, E.; Gomes, S. D.; Toulme, J. J. *Curr. Opin. Pharmacol.* **2009**, *9*, 602.

(23) Willner, I.; Zayats, M. *Angew. Chem. Int. Edit.* **2007**, *46*, 6408.

(24) Xu, Y.; Yang, L.; Ye, X. Y.; He, P. A.; Fang, Y. Z. *Electroanalysis* **2006**, *18*, 1449.

(25) Lin, J. C.; Thirumalai, D. *J. Am. Chem. Soc.* **2008**, *130*, 14080.

(26) Mayer, G. *Angew. Chem. Int. Ed.* **2009**, *48*, 2672.

(27) Ellington, A. D.; Szostak, J. W. *Nature* **1992**, *355*, 850.

(28) Cox, J. C.; Ellington, A. D. *Biorg. Med. Chem.* **2001**, *9*, 2525.

(29) Nutiu, R.; Li, Y. F. *Angew. Chem.-Int. Edit.* **2005**, *44*, 1061.

(30) Ruff, K. M.; Snyder, T. M.; Liu, D. R. *J. Am. Chem. Soc.* **2010**, *132*, 9453.

(31) Miyachi, Y.; Shimizu, N.; Ogino, C.; Kondo, A. *Nucleic Acids Res.* **2010**, *38*, e21.

(32) Stratis-Cullum, D. N.; McMasters, S.; Pellegrino, P. M. *Anal. Lett.* **2009**, *42*, 2389.

(33) Osborne, S. E.; Ellington, A. D. *Chem. Rev.* **1997**, *97*, 349.

(34) Yang, Y.; Yang, D. L.; Schluesener, H. J.; Zhang, Z. R. *Biomol. Eng.* **2007**, *24*, 583.

(35) Hamula, C. L. A.; Guthrie, J. W.; Zhang, H. Q.; Li, X. F.; Le, X. C. *TrAC, Trends Anal. Chem.* **2006**, *25*, 681.

(36) Sam, M.; Boon, E. M.; Barton, J. K.; Hill, M. G.; Spain, E. M. *Langmuir* **2001**, *17*, 5727.

(37) Kelley, S. O.; Barton, J. K.; Jackson, N. M.; McPherson, L. D.; Potter, A. B.; Spain, E. M.; Allen, M. J.; Hill, M. G. *Langmuir* **1998**, *14*, 6781.

(38) Herne, T. M.; Tarlov, M. J. *J. Am. Chem. Soc.* **1997**, *119*, 8916.

(39) Radi, A.-E.; Sánchez, J. L. A.; Baldrich, E.; O'Sullivan, C. K. *Anal. Chem.* **2005**, *77*, 6320.

(40) Lai, R. Y.; Seferos, D. S.; Heeger, A. J.; Bazan, G. C.; Plaxco, K. W. *Langmuir* **2006**, *22*, 10796.

(41) White, R. J.; Phares, N.; Lubin, A. A.; Xiao, Y.; Plaxco, K. W. *Langmuir* **2008**, *24*, 10513

(42) Ge, B.; Huang, Y.-C.; Sen, D.; Yu, H.-Z. *J. Electroanal. Chem.* **2007**, *602*, 156.

(43) Steel, A. B.; Herne, T. M.; Tarlov, M. J. *Anal. Chem.* **1998**, *70*, 4670.

(44) Kaiser, W.; Rant, U. *J. Am. Chem. Soc.* **2010**, *132*, 7935.

(45) Lao, R.; Song, S.; Wu, H.; Wang, L.; Zhang, Z.; He, L.; Fan, C. *Anal. Chem.* **2005**, *77*, 6475.

(46) Peterson, A. W.; Heaton, R. J.; Georgiadis, R. M. *Nucleic Acids Res.* **2001**, *29*, 5163.

(47) Ricci, F.; Lai, R. Y.; Heeger, A. J.; Plaxco, K. W.; Sumner, J. J. *Langmuir* **2007**, *23*, 6827.

(48) Razumovitch, J.; de França, K.; Kehl, F.; Wiki, M.; Meier, W.; Vebert, C. *J. Phys. Chem. B* **2009**, *113*, 8383.

(49) Cheng, A. K. H.; Ge, B.; Yu, H.-Z. *Anal. Chem.* **2007**, *79*, 5158.

(50) Kelley, S. O.; Barton, J. K. *Science* **1999**, *283*, 375.

(51) Kelley, S. O.; Jackson, N. M.; Hill, M. G.; Barton, J. K. *Angew. Chem. Int. Ed.* **1999**, *38*, 941.

(52) Boon, E. M.; Jackson, N. M.; Wightman, M. D.; Kelley, S. O.; Hill, M. G.; Barton, J. K. *J. Phys. Chem. B* **2003**, *107*, 11805.

(53) Elias, B.; Shao, F.; Barton, J. K. *J. Am. Chem. Soc.* **2008**, *130*, 1152.

(54) Genereux, J. C.; Barton, J. K. *Chem. Rev.* **2010**, *110*, 1642.

(55) Kelley, S. O.; Barton, J. K. *Chemistry & Biology* **1998**, *5*, 413.

(56) Holmlin, R. E.; Tong, R. T.; Barton, J. K. *J. Am. Chem. Soc.* **1998**, *120*, 9724.

(57) Genereux, J. C.; Wuerth, S. M.; Barton, J. K. *J. Am. Chem. Soc.* **2011**, *133*, 3863.

(58) Slinker, J. D.; Muren, N. B.; Renfrew, S. E.; Barton, J. K. *Nat. Chem.* **2011**, *3*, 230.

(59) Anne, A.; Bouchardon, A.; Moiroux, J. *J. Am. Chem. Soc.* **2003**, *125*, 1112.

(60) Anne, A.; Demaille, C. *J. Am. Chem. Soc.* **2005**, *128*, 542.

(61) Wang, K.; Goyer, C.; Anne, A.; Demaille, C. *J. Phys. Chem. B* **2007**, *111*, 6051.

(62) Uzawa, T.; Cheng, R. R.; White, R. J.; Makarov, D. E.; Plaxco, K. W. *J. Am. Chem. Soc.* **2010**, *132*, 16120.

(63) Balamurugan, S.; Obubuafo, A.; Soper, S. A.; Spivak, D. A. *Anal. Bioanal. Chem.* **2008**, *390*, 1009.

(64) *Integrated DNA Technologies*; Integrated DNA Technologies, Inc.: www.idtdna.com, 2011.

(65) *Eurofins MWG Operon*; www.operon.com: Eurofins MWG Operon, 2011.

(66) Paleček, E.; Fojta, M.; Jelen, F.; Vetterl, V. In *Bioelectrochemistry*; Wilson, G. S., Ed.; Wiley-VCH Verlag GmbH: Weinheim, 2002; Vol. 9, p 365

(67) Polsky, R.; Gill, R.; Kaganovsky, L.; Willner, I. *Anal. Chem.* **2006**, *78*, 2268.

(68) Hansen, J. A.; Wang, J.; Kawde, A.-N.; Xiang, Y.; Gothelf, K. V.; Collins, G. *J. Am. Chem. Soc.* **2006**, *128*, 2228.

(69) Yang, H.; Ji, J.; Liu, Y.; Kong, J. L.; Liu, B. H. *Electrochem. Comm.* **2009**, *11*, 38.

(70) Ikebukuro, K.; Kiyohara, C.; Sode, K. *Anal. Lett.* **2004**, *37*, 2901.

(71) Harrison, D. C. *Biochem. J.* **1931**, *25*, 1016.

(72) Tasset, D. M.; Kubik, M. F.; Steiner, W. *J. Mol. Bio.* **1997**, *272*, 688.

(73) Ikebukuro, K.; Kiyohara, C.; Sode, K. *Biosens. Bioelectron.* **2005**, *20*, 2168.

(74) Sode, K.; Kojima, K. *Biotechnol. Lett.* **1997**, *19*, 1073.

(75) Centi, S.; Bonel Sanmartin, L.; Tombelli, S.; Palchetti, I.; Mascini, M. *Electroanalysis* **2009**, *21*, 1309.

(76) Lavie, C. J.; Milani, R. V.; Verma, A.; O'Keefe, J. H. *Am. J. Med. Sci.* **2009**, *338*, 486.

(77) Wang, K. Y.; McCurdy, S.; Shea, R. G.; Swaminathan, S.; Bolton, P. H. *Biochemistry* **1993**, *32*, 1899.

(78) Macaya, R. F.; Waldron, J. A.; Beutel, B. A.; Gao, H. T.; Joesten, M. E.; Yang, M. H.; Patel, R.; Bertelsen, A. H.; Cook, A. F. *Biochemistry* **1995**, *34*, 4478.

(79) Radi, A.-E.; Acero Sánchez, J. L.; Baldrich, E.; O'Sullivan, C. K. *J. Am. Chem. Soc.* **2005**, *128*, 117.

(80) Baldrich, E.; Restrepo, A.; O'Sullivan, C. K. *Anal. Chem.* **2004**, *76*, 7053.

(81) Sánchez, J.; Baldrich, E.; Radi, A. G.; Dondapati, S.; Sánchez, P.; Katakis, I.; O'Sullivan, C. *Electroanalysis* **2006**, *18*, 1957.

(82) Xiao, Y.; Lubin, A. A.; Heeger, A. J.; Plaxco, K. W. *Angew. Chem. Int. Ed.* **2005**, *44*, 5456

(83) Xiao, Y.; Uzawa, T.; White, R. J.; DeMartini, D.; Plaxco, K. W. *Electroanalysis* **2009**, *21*, 1267.

(84) Stojanovic, M. N.; de Prada, P.; Landry, D. W. *J. Am. Chem. Soc.* **2000**, *122*, 11547.

(85) Baker, B. R.; Lai, R. Y.; Wood, M. S.; Doctor, E. H.; Heeger, A. J.; Plaxco, K. W. *J. Am. Chem. Soc.* **2006**, *128*, 3138.

(86) Swensen, J. S.; Xiao, Y.; Ferguson, B. S.; Lubin, A. A.; Lai, R. Y.; Heeger, A. J.; Plaxco, K. W.; Soh, H. T. *J. Am. Chem. Soc.* **2009**, *131*, 4262.

(87) Stojanovic, M. N.; de Prada, P.; Landry, D. W. *J. Am. Chem. Soc.* **2001**, *123*, 4928.

(88) Zuo, X.; Song, S.; Zhang, J.; Pan, D.; Wang, L.; Fan, C. *J. Am. Chem. Soc.* **2007**, *129*, 1042.

(89) Lu, Y.; Li, X.; Zhang, L.; Yu, P.; Su, L.; Mao, L. *Anal. Chem.* **2008**, *80*, 1883.

(90) Sankar, C. G.; Sen, D. *Journal of Molecular Biology* **2004**, *340*, 459.

(91) Huang, Y. C.; Ge, B.; Sen, D.; Yu, H.-Z. *J. Am. Chem. Soc.* **2008**, *130*, 8023.

(92) Kelly, J. A.; Feigon, J.; Yeates, T. O. *J. Mol. Bio.* **1996**, *256*, 417.

(93) Rodriguez, M. C.; Kawde, A.-N.; Wang, J. *Chem. Comm.* **2005**, 4267.

(94) Cai, H.; Lee, T. M.-H.; Hsing, I. M. *Sens. Actuators, B* **2006**, *114*, 433.

(95) Zhang, Z.; Yang, W.; Wang, J.; Yang, C.; Yang, F.; Yang, X. *Talanta* **2009**, *78*, 1240.

(96) Gendler, S.; Taylor-Papadimitriou, J.; Duhig, T.; Rothbard, J.; Burchell, J. *J. Biol. Chem.* **1988**, *263*, 12820

(97) Wei, X.; Xu, H.; Kufe, D. *Cancer Cell* **2005**, *7*, 167.

(98) Wei, X.; Xu, H.; Kufe, D. *Cancer Res.* **2007**, *67*, 1853.

(99) Carson, D. D. *Sci. Signal.* **2008**, *1*, pe35.

(100) Bon, G. G.; von Mensdorff-Pouilly, S.; Kenemans, P. van Kamp, G. J.; Verstraeten, R. A.; Hilgers, J.; Meijer, S.; Vermorken, J. B. *Clin. Chem.* **1997**, *43*, 585 – 593.

(101) Price, M. R.; Hudecz, F.; O'Sullivan, C.; Baldwin, R. W.; Edwards, P. M.; Tendler, S. J. B. *Mol. Immunol.* **1990**, *27*, 795 – 802.

(102) Cheng, A. K. H.; Su, H.; Wang, Y. A.; Yu, H.-Z. Anal. Chem. **2009,** *81*, 6130.

(103) Ferreira, C. S.; Matthews, C. S.; Missailidis, S. *Tumour Biol.* **2006**, *27*, 289.

(104) *mfold Web Server* http://www.bioinfo.rpi.edu/applications/mfold, 2010.

(105) M. Zuker, Mfold web server for nucleic acid folding and hybridization prediction. *Nucleic Acids Res.* 2003, *31*. 3406 - 3415.

(106) Ferreira, C. S. M.; Papamichael, K.; Guilbault, G.; Schwarzacher, T.; Gariepy, J.; Missailidis, S. *Anal. Bioanal. Chem.* **2008**, *390*, 1039.

(107) Sambrook, J.; Russell, D. W. In *Molecular Cloning: A Laboratory Manual*; 3rd ed.; Cold Spring Harbor Laboratory Press: 2001; Vol. 2, p 10.11

(108) Thomas, J., Personal communications.

(109) Scopes, R. K. *Anal. Biochem.* **1974**, *59*, 277

(110) Sambrook, J.; Russell, D. W. In *Molecular Cloning: A Laboratory Manual*; 3rd ed.; Cold Spring Harbor Laboratory Press: 2001; Vol. 2, p 10.17

(111) Piccardoni, P.; Evangelista, V.; Piccoli, A.; de Gaetano, G.; Walz, A.; Cerletti, C. *Thromb. Haemost.* **1996**, *76*, 780

(112) Hellman, L. M.; Fried, M. G. *Nat. Protocols* **2007**, *2*, 1849.

(113) Revzin, A. *J. Chem. Educ.* **1990**, *67*, 749.

(114) Famulok, M.; Mayer, G.; Blind, M. *Acc. Chem. Res.* **2000**, *33*, 591.

(115) Tombelli, S.; Minunni, M.; Mascini, M. *Biosens. Bioelectron.* **2005**, *20*, 2424.

(116) Henning, U.; Carsten, W. *Cytometry Part A* **2009**, *75A*, 727.

(117) Lubin, A. A.; Plaxco, K. W. *Acc. Chem. Res.* **2010**, *43*, 496.

(118) Ho, C.; Yu, H.-Z. In *Neuromethods*; Marinesco, S., Ed.; Humana Press: In Press.

(119) Anne, A.; Bonnaudat, C.; Demaille, C.; Wang, K. *J. Am. Chem. Soc.* **2007**, *129*, 2734.

(120) Zhan, R.; Song, S.; Liu, Y.; Dong, S. *J. Chem. Soc., Faraday Trans.* **1990,** *86*. 3125 - 3127.

(121) Irving, D.; Gong, P.; Levicky, R. *J. Phys. Chem. B* **2010**, *114*, 7631.

(122) Satjapipat, M.; Sanedrin, R.; Zhou, F. *Langmuir* **2001**, *17*, 7637.

(123) Arinaga, K.; Rant, U.; Knezevic, J.; Pringsheim, E.; Tornow, M.; Fujita, S.; Abstreiter, G.; Yokoyama, N. *Biosens. Bioelectron.* **2007**, *23*, 326.

(124) Henry, O. Y. F.; Perez, J. G.; Sanchez, J. L. A.; O'Sullivan, C. K. *Biosens. Bioelectron.* **2010**, *25*, 978.

(125) Laviron, E. *J. Electroanal. Chem.* **1979**, *101*, 19.

(126) Yu, H.-Z.; Luo, C.-Y.; Sankar, C. G.; Sen, D. *Anal. Chem.* **2003**, *75*, 3902.

(127) Anne, A.; Demaille, C. *J. Am. Chem. Soc.* **2008**, *130*, 9812.